Chromodynamic multirelaxation-time lattice Boltzmann scheme for fluids with density difference

J. Spendlove,[1] X. Xu,[1,2] O. J. Halliday,[3] T. Schenkel,[1,2] and I. Halliday[1]

[1]*Materials & Engineering Research Institute, Sheffield Hallam University, Howard Street, Sheffield S1 1WB, United Kingdom*
[2]*Department of Engineering and Mathematics, Sheffield Hallam University, Howard Street, Sheffield S1 1WB, United Kingdom*
[3]*National Centre for Atmospheric Science, Department of Meteorology, University of Reading, Reading RG6 6AH, United Kingdom*

We develop, after Dellar [Phys. Rev. E. **65**, 036309 (2002); J. Comput. Phys. **190**, 351 (2003)], a multiple-relaxation-time (MRT), chromodynamic, multicomponent lattice Boltzmann equation (MCLBE) scheme for simulation of isothermal, immiscible fluid flow with a density contrast. It is based on Lishchuk's method [Brackbill, Kothe, and Zemach, J. Comp. Phys. **100**, 335 (1992); Lishchuk, Care, and Halliday, Phys. Rev. E. **67**, 036701, (2003)] and the segregation of d'Ortona *et al.* [Phys. Rev. E. **51**, 3718, (1995)]. We focus on fundamental model verifiability but do relate some of our data to that from previous approaches, due to Ba *et al.* [Phys. Rev. E **94**, 023310 (2016)] and earlier Liu *et al.* [Phys. Rev. E **85**, 046309 (2012)], who pioneered large density difference chromodynamic MCLBE and showed the practical benefits of an MRT collision model. Specifically, we test the extent to which chromodynamic MCLBE MRT schemes comply with the kinematic condition of mutual impenetrability and the continuous traction condition by developing analytical benchmarking flows. We conclude that our data, taken with those of Ba *et al.*, verify the utility of MRT chromodynamic MCLBE.

I. INTRODUCTION

Since 1991, when Gunstensen and Rothman [1] invented the technique, several multicomponent lattice Boltzmann equation (MCLBE) variants have been developed to address different flow regimes [2–4]. The idea remains a milestone of statistical physics; however, all current MCLBE variants depart substantially from Ref. [1], which developed directly from Rothman's earlier immiscible lattice gas cellular automata [5,6].

Presently, variants are classified by their physical content [7]. Where the kinetics of phase separation must be considered, "free-energy" methods [8,9] and their thermodynamically consistent extensions, due to Wagner *et al.* [10–12], are appropriate tools. For workers with a background in molecular simulation, the Shan-Chen method [13] is a natural choice. In continuum immiscible hydrodynamics, one incorporates dynamic conditions of stress continuity (i.e., physical principles) and the kinematic condition of mutual impenetrability (with purely logical content) [14] as boundary conditions between separate flows. In this regime it is safe to use the chromodynamic, color-gradient, or phase-field method, which we define as a combination of algorithms due to Lishchuk [15] (who uses earlier ideas of Brackbill, [16]) and d'Ortona *et al.* [17].

Chromodynamic MCLBE uses an immersed boundary force [16,18], appropriate corrections being applied to the velocity [19], alongside a computationally efficient, analytic component segregation [17] which distributes an interface, which, for continua, should be sharp. (Note, Reiss and Phillips [20] developed an interfacial perturbation to replace immersed boundary forces, which is the most physically consistent encapsulation of MCLB interfacial tension as a perturbation to the stress.) The method is the most direct descendant of Gunstensen's original, in which the problems of lattice pinning and faceting have been reduced, Reiss and Dellar [21,22] having identified their origin and a means to reduce the impact of the unphysical interface width scale. Such limitations notwithstanding, chromodynamic method is robust, transparent, has low microcurrent and allows direct parametrization of interfacial tension, width [23], and the separated fluids' viscosity contrast [24], the interface propagation in the base model is reasonably understood [25,26] (but see below) and different color gradient (CG) models have been applied successfully to numerical study of steady and unsteady flow [27–30].

Here we further investigate the fundamentals of the dynamics and kinematics of a chromodynamic MCLB interface, when it separates fluids at density ratio Λ. Our data aim to support results by Ba *et al.* [29] and Wen *et al.* [30], who have benchmarked the technique in complex flow situations using multirelaxation-time (MRT) collision schemes and generalizations of the segregation method of Ref. [17].

Use of an MRT collision scheme complicates the relationship between model kinematics (which originate in the recolor step—see Sec. II) and model dynamics (which is extracted by Chapman-Enskog analysis) [31]. But MRT schemes have the decisive advantage of stability. Hence, we develop a Dellar-type MRT scheme, for chromodynamic MCLBE which couples model kinematics and dynamics clearly. Taking this model as representative of chromodymamic MRT schemes, we extend previous work [31], to measure the extent to which such models meet appropriate dynamic and kinematic conditions. To achieve this, one should consider fully transient flows. We do so, first with plane and, later, curved interfaces. By making direct comparison with appended semianalytic calculations, which invoke kinematic and dynamic conditions,
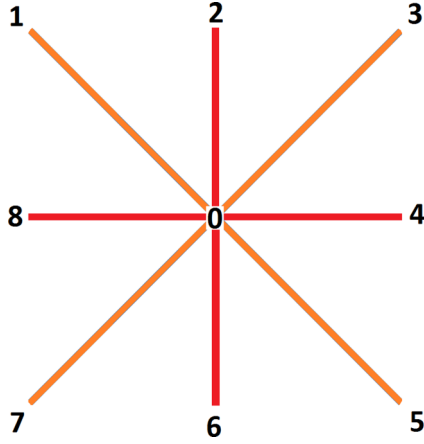
FIG. 1. Schematic. Square $D2Q9$ lattice with our indexing convention. Odd values of i identify the longer links.

we answer the questions to what extent do the lattice fluids move together at the interface? and to what extent is the continuous traction condition met?

We organize the paper as follows. In Sec. II we present background detail of our model; in Sec. III we derive an MRT scheme for it; in Sec. IV we present and use semianalytic tests alongside refined versions of existing tests, to assess its performance. In Sec. V, we present our conclusions. Details are presented in the Appendices.

II. BACKGROUND: DENSITY DIFFERENCE CHROMODYNAMIC MCLBE

Represent red and blue fluid components by distribution functions $R_i(\mathbf{r}, t)$ and $B_i(\mathbf{r}, t)$, where

$$f_i(\mathbf{r}, t) = R_i(\mathbf{r}, t) + B_i(\mathbf{r}, t). \tag{1}$$

Above, $i = 0, 1, .., (Q-1)$ indexes the Q lattice links in the model (Fig. 1). Let $\rho = (\rho_R + \rho_B)$, ρ_R, ρ_B, δ_t, $c_{i\alpha}$, w_i, u, and c_s denote nodal density, red nodal density, blue nodal density, time step, the α component of the ith lattice basis vector, the weight for link i, fluid velocity, and the color-blind speed of sound (or the geometrical lattice tensor isotropy constant), respectively. Other symbols have their usual meanings. An MRT collision scheme, for a single fluid subject to a body force, $G_\alpha(\mathbf{r})$, has a kinetic equation

$$f_i(\mathbf{r} + \delta_t \mathbf{c}_i, t + \delta_t) = f_i(\mathbf{r}, t) - \sum_{j=0}^{Q-1} A_{ij}[f_j(\mathbf{r}, t) - f_j^{(0)}(\rho, \mathbf{u})]$$
$$+ F_{1i} + F_{2i}, \tag{2}$$

where, after Refs. [29,30], equilibrium $f_i^{(0)}$ is modified to allocate mass away from rest link ($i = 0$), generating a density contrast [29,30,32]:

$$f_i^{(0)}(\rho, \mathbf{u}) = \rho \phi_i + w_i \rho \left(\frac{u_\alpha c_{i\alpha}}{c_s^2} + \frac{u_\alpha u_\beta c_{i\alpha} c_{i\beta}}{2c_s^4} - \frac{u^2}{2c_s^2} \right), \tag{3}$$

with

$$\phi_i = \begin{cases} \frac{\alpha_R \rho_R}{\rho} + \frac{\alpha_B \rho_B}{\rho}, & i = 0, \\ k w_i [(1 - \alpha_R) \frac{\rho_R}{\rho} + (1 - \alpha_B) \frac{\rho_B}{\rho}], & i \neq 0, \end{cases} \tag{4}$$

where $k = \frac{9}{5}$, in $D2Q9$. Above, α_R and α_B are considered shortly when discussing the role of ϕ_i.

In Eq. (2), A_{ij} is a collision matrix element and "sources" F_{1i} and F_{2i} correct the dynamics for the effects of large density contrasts and $\mathbf{G}$, respectively [31]. Term F_{1i} is expressed in tensor Hermite polynomials,

$$F_{1i} = w_i T_{\alpha\beta}(\rho_R, \rho_B, \rho^N, \Lambda, \mathbf{u})(c_{i\alpha} c_{i\beta} - c_s^2 \delta_{\alpha\beta}), \tag{5}$$

and to embed $\mathbf{G}$ we use the form devised by Luo [33],

$$F_{2i} = w_i \left[\frac{\mathbf{G} \cdot \mathbf{c}_{i\alpha}}{c_s^2} + \frac{1}{2c_s^4} \left(1 - \frac{\lambda_3}{2} \right) \right.$$
$$\left. \times (G_\alpha u_\beta + G_\beta u_\alpha)(c_{i\alpha} c_{i\beta} - c_s^2 \delta_{\alpha\beta}) \right]. \tag{6}$$

Term $T_{\alpha\beta}$ and eigenvalue λ_3 (which determines lattice fluid kinematic viscosity) are considered in Appendix A. Note, we assume force-adjusted macroscopic observables,

$$(\rho_R, \rho_B) = \sum_i (R_i, B_i), \quad \mathbf{u} = \frac{\sum_i f_i(\mathbf{r}, t)\mathbf{c}_i}{\rho} + \frac{\mathbf{G}}{2\rho}. \tag{7}$$

Return now to the density contrast mechanism embedded in $f_i^{(0)}$ and F_{1i}. Parameters α_R and α_B are chosen such that

$$\Lambda = \frac{\rho_{0R}}{\rho_{0B}} = \frac{c_{sB}^2}{c_{sR}^2} = \left(\frac{1 - \alpha_B}{1 - \alpha_R} \right), \tag{8}$$

i.e., to control density contrast, Λ, via the sonic speed. Equation (8) supports a condition for mechanical stability, $\rho_{0R} c_{SR}^2 = \rho_{0B} c_{SB}^2$, where ρ_{0C} is the density deep within the component $C = R, B$.

Components are identified by a color index $\rho^N(\mathbf{r}, t)$,

$$\rho^N(\mathbf{r}, t) \equiv \frac{\left(\frac{\rho_R(\mathbf{r},t)}{\rho_{0R}} - \frac{\rho_B(\mathbf{r},t)}{\rho_{0B}} \right)}{\left(\frac{\rho_R(\mathbf{r},t)}{\rho_{0R}} + \frac{\rho_B(\mathbf{r},t)}{\rho_{0B}} \right)} \in [-1, 1] \tag{9}$$

[29,30,32], in terms of which interfacial tension is created by the action of force,

$$\mathbf{G} = \tfrac{1}{2} \sigma K \nabla \rho^N, \tag{10}$$

where σ is the interfacial tension and the mean curvature is measured as follows [16]:

$$K = \underline{\nabla} \cdot \hat{n}, \quad \hat{n} = -\left(\frac{\nabla \rho^N}{|\nabla \rho^N|} \right), \tag{11}$$

for a red drop, with the usual convention on surface normal, $\hat{n}$. Color field ρ^N is considered continuous, changing rapidly only in the interfacial region. Its variation may be sharpened [21,22] and it may be used to control kinematic viscosity, by setting $\nu(\rho^N) = \frac{1}{6}(\frac{2}{\lambda_3(\rho^N)} - 1)$ [24,34]. Kinetic-scale, post-collision color segregation is an adaptation of Ref. [17],

$$C_i^{++}(\mathbf{r}, t) = \frac{\rho_C(\mathbf{r}, t)}{\rho(\mathbf{r}, t)} f_i(\mathbf{r}, t)^+$$
$$\pm \beta \frac{\phi_i(\mathbf{r}, t) \rho_R(\mathbf{r}, t) \rho_B(\mathbf{r}, t)}{\rho(\mathbf{r}, t)} \hat{\mathbf{n}} \cdot \delta_t \hat{\mathbf{c}}_i, \tag{12}$$

where superscript $+$ ($++$) denotes a post-collision (post-recolor) quantity and β is a chosen parameter [17]. This simple segregation rule is mass-conserving, local (given a director, $\hat{\mathbf{n}}$) and "bottom-up," i.e., a kinetic scale postulate. It

is usually ignored in deriving macroscopic model behavior. However, Eq. (12) is consistent with a modified equation for uniform fluid motion [31],

$$
\frac{D\rho_R}{Dt} + \frac{1}{2}\delta_t \frac{\partial^2 \rho_R}{\partial t^2}
$$

$$
= \frac{k}{2}c_s^2(1-\alpha_R)\delta_t \nabla^2\left(\frac{\rho_R^2}{\rho}\right) + \frac{k}{2}c_s^2(1-\alpha_B)\delta_t \nabla^2\left(\frac{\rho_R\rho_B}{\rho}\right)
$$

$$
+ \frac{1}{2}\delta_t u_\alpha u_\beta \partial_\alpha \partial_\beta \rho_R - \delta_t \beta(1-\alpha_R)kc_s^2 n_\gamma \partial_\gamma\left(\frac{\rho_R^2 \rho_B}{\rho^2}\right)
$$

$$
- \delta_t \beta(1-\alpha_B)kc_s^2 n_\gamma \partial_\gamma\left(\frac{\rho_R \rho_B^2}{\rho^2}\right) + 2\delta_t c_s^4 \partial_\alpha \partial_\beta\left(\frac{\rho_R T_{\alpha\beta}}{\rho}\right).
$$

(13)

Above, the last term on the right-hand side originates in correction term, F_{1i} [see Eq. (5)]. Burgin *et al.* [31] give this term for an LBGK collision model; on neglecting it they find by solving Eq. (13): $\rho_R(\mathbf{r},t) = \frac{\rho_{0R}}{2}(1 + \tanh(\beta\hat{\mathbf{n}} \cdot (\mathbf{r} - \mathbf{u}t)))$, with equivalent behavior for ρ_B. When substituted in Eq. (9), these variations reveal a smoothly varying color index:

$$
\rho^N(\mathbf{r},t) = \tanh\left[\beta\hat{\mathbf{n}} \cdot (\mathbf{r} - \mathbf{u}t)\right].
$$

(14)

Quantity ρ^N is a material invariant, at leading order—see below. However, the last term in Eq. (13) constitutes an error associated with pure advection, present even in uniform flow, which is shown to restrict applicability of the method.

As remarked above, taking the order δ_t terms in Eq. (13),

$$
\frac{\partial \rho_R}{\partial t} + u_\gamma \partial_\gamma \rho_R \approx 0, \quad \frac{\partial \rho_B}{\partial t} + u_\gamma \partial_\gamma \rho_B \approx 0, \quad (15)
$$

which is useful in deriving our MRT scheme, in Sec. III, where Eq. (15) is taken to imply that on short timescales, t_0, the color index is an approximate material invariant, which eliminates its t_0 derivatives from the Euler equation.

Note, Eqs. (5), (6), and (10) require numerical gradients. Typically, compact second-order stencils, relying on lattice isotropies, are found to be sufficient in MCLBE but higher order, noncompact versions (see Appendix B) are helpful here.

III. MRT SCHEME FOR LARGE DENSITY DIFFERENCE CHROMODYNAMIC MCLBE

Dellar [35,36] developed an MRT scheme for single component flow, which was extended to accommodate the force, **G**, used in chromodynamic lattice Boltzmann multicomponent flow [24]. Here, we further adapt that method to completely immiscible fluids, with density contrast Λ, where it is necessary to consider large density gradients in the region of rapidly changing ρ^N.

Dellar's is arguably the most aesthetic and logically consistent MRT scheme. **A** is defined by its eigenvalues and eigenvectors, only a subset of which must be chosen, a majority being assigned in the Chapman-Enskog process. Working from a weighted orthogonal modal basis introduced by Junk [37], Dellar [35,36] devised an MRT scheme with less coupling between the density, momentum, and stress modes and the three "ghost" modes (in $D2Q9$) than is present in the more commonly used MRT scheme of Lallemand and Luo [38].

We derive, in Appendix A, an MRT scheme-based model, generalized to chromodynamic immiscible fluids. Our analysis, performed in $D2Q9$, attempts to clarify the coupling between collision and model kinematics. See also Ref. [31]. The resulting scheme involves a set of macroscopic modes, $\mathbf{h}^{(p)}$, defined in Table I; a majority representing observables, e.g., momentum components.

We define a projection matrix, comprised of orthogonal left row collision matrix eigenvectors, $\mathbf{h}^{(p)}$, each a projector of a particular mode, $m^{(p)}$,

$$
\mathbf{M} \equiv (\mathbf{h}^{(0)}, \mathbf{h}^{(1)}, \cdots, \mathbf{h}^{(8)})^T,
$$

such that

$$
(m^{(0)}, m^{(1)}, ..., m^{(8)})^T = \mathbf{M}\,\mathbf{f}
$$
$$
= \left(\rho, \rho u_x, \rho u_y, \sigma_{xx}, \sigma_{yy}, \sigma_{xy}, N, J_x, J_y\right)^T
$$

(see Table I). Above, column vector $\mathbf{f} \equiv (f_0, f_1, ..., f_8)^T$. We define all the $\mathbf{h}^{(p)}$ as weighted polynomial expressions in the lattice basis of Fig. 1, because a subset (of the $\mathbf{h}^{(p)}$) are naturally identified as such when deriving the dynamics; see Appendix A. Project Eq. (2) using left multiplication by $\mathbf{M}$,

$$
\mathbf{M}\,\mathbf{f}^+ = \mathbf{M}\,\mathbf{f} + \mathbf{M}\,\mathbf{A}\,\mathbf{M}^{-1}(\mathbf{M}\,\mathbf{f}^{(0)} - \mathbf{M}\,\mathbf{f}) + \mathbf{M}\,\mathbf{F}, \quad (16)
$$

TABLE I. Collision matrix eigenspectrum summary and notation. Left row eigenvectors (projectors), $\mathbf{h}^{(p)}(p = 0, 1, ..., 8)$, corresponding (i) mode $m^{(p)} \equiv \sum_i h_i^{(p)} f_i$, (ii) eigenvalue, (iii) physical significance, and (iv) equilibrium.

Eigenvector	Component	Definition	Eigenvalue, λ_p	Mode, $m^{(p)}$	Physical interpretation	Equilibrium, $m^{(0)(p)}$
$\mathbf{h}^{(0)}$	$h_i^{(0)}$	w_i	0	ρ	Density	ρ
$\mathbf{h}^{(1)}$	$h_i^{(1)}$	$w_i c_{ix}$	0	ρu_x	x momentum	ρu_x
$\mathbf{h}^{(2)}$	$h_i^{(2)}$	$w_i c_{iy}$	0	ρu_y	y momentum	ρu_y
$\mathbf{h}^{(3)}$	$h_i^{(3)}$	$w_i c_{ix}^2$	λ_3	Π_{xx}	Momentum flux component	$\Pi_{xx}^{(0)}$
$\mathbf{h}^{(4)}$	$h_i^{(4)}$	$w_i c_{iy}^2$	λ_3	Π_{yy}	Momentum flux component	$\Pi_{yy}^{(0)}$
$\mathbf{h}^{(5)}$	$h_i^{(5)}$	$w_i c_{ix} c_{iy}$	λ_3	Π_{xy}	Momentum flux component	$\Pi_{xy}^{(0)}$
$\mathbf{h}^{(6)}$	$h_i^{(6)}$	g_i	λ_6	N	–	0
$\mathbf{h}^{(7)}$	$h_i^{(7)}$	$g_i c_{ix}$	λ_7	J_x	–	0
$\mathbf{h}^{(8)}$	$h_i^{(8)}$	$g_i c_{iy}$	λ_7	J_y	–	0

where $\mathbf{F}$ is the column vector whose elements are $F_i = F_{1i} + F_{2i}$. The projected evolution equation decomposes to forced scalar relaxations for each mode,

$$m^{(p)+} = m^{(p)} + \lambda_p(m^{(0)(p)} - m^{(p)}) + S^{(p)},$$

$$S^{(p)} = \sum_{j=0}^{8} M_{pj}F_j, \quad p = 0, 1, 2, ..., (Q-1). \quad (17)$$

In Eq. (17), we use the properties of the $\mathbf{h}^{(p)}$, from which $\mathbf{M\,A} = \boldsymbol{\Lambda\,M}$, i.e., $\boldsymbol{\Lambda} = \mathbf{M\,A\,M^{-1}}$, with $\boldsymbol{\Lambda} \equiv \mathrm{diag}(\lambda_0, \lambda_1, ..., \lambda_8)$. Note, zero eigenvalues are associated with physical modes subject to conservation principles.

Developing an MRT scheme now reduces to specifying equilibria, $m^{(0)(p)}$, and sources $S^{(p)}$, such that a Chapman-Enskog expansion of the kinetic scale dynamics predicts that the physical modes (Table I) conform with the continuity and Navier-Stokes equations; see Appendix A.

An advantage of Dellar's approach is that $\mathbf{M}$ may be inverted, using lattice isotropies. The modal evolutions in Eq. (17) are inverted to yield $\mathbf{f}^+ = \mathbf{M^{-1}\,m^+}$. So the post-collision distribution function is constructed directly from post-collision $m^{(p)+}$,

$$
\begin{aligned}
f_i^+ &= (M)_{ij}^{-1}\,m_j^+ \\
&= w_i\Bigg\{\left[2 - \frac{3}{2}\big(c_{ix}^2 + c_{iy}^2\big)\right]\rho + 3((\rho u_x)^+ c_{ix} + (\rho u_y)^+ c_{iy}) \\
&\quad + \frac{9}{2}\big(\Pi_{xx}^+ c_{ix}^2 + 2\Pi_{xy}^+ c_{ix}c_{iy} + \Pi_{yy}^+ c_{iy}^2\big) - \frac{3}{2}(\Pi_{xx}^+ + \Pi_{yy}^+) \\
&\quad + \frac{1}{4}g_i N^+ + \frac{3}{8}g_i(J_x^+ c_{ix} + J_y^+ c_{iy})\Bigg\},
\end{aligned}
$$

with $(\rho u_x)^+$, $(\rho u_y)^+$, ρ^+, Π_{xx}^+, Π_{xy}^+, Π_{yy}^+, N^+, J_x^+, and J_y^+ given explicitly in Eqs. (A36)–(A41). Of course, color is finally reallocated according to Eq. (12).

Tensor $T_{\alpha\beta}$ in Eqs. (5) and (13) is shown, in Appendix A, Eq. (A29), to be identical to that of Burgin *et al.* [31], for an LBGK model.

IV. RESULTS AND DISCUSSION

The accuracy of our multicomponent scheme of Sec. III is assessed against the conditions of mutual impenetrability (model kinematics) and the viscous stress transmission (model dynamics). Transfer of momentum between immiscible fluids is controlled by boundary conditions which refer to both kinematics and dynamics. In Appendix C we present two transient test-bench flows which rely upon these conditions which we compare with data. We mainly consider here the dynamics of the scheme, its kinematics having been effectively assessed by Burgin *et al.* [31], on the following argument.

Whilst the work of Burgin *et al.* uses an LBGK collision method (to highlight the connection between the model kinematics and dynamics), the key tests applied consider performance in uniform flow, with a flat interface i.e., $\mathbf{G} = \mathbf{0}$. In this regime, there is no practical distinction between the operation of MRT and LBGK schemes. Put another way, Burgin's simulation data applies to the chromodynamic MCLBE MRT method of Sec. III. (note, however, we have confirmed this explicitly). Moreover, the kinetic equation source due from
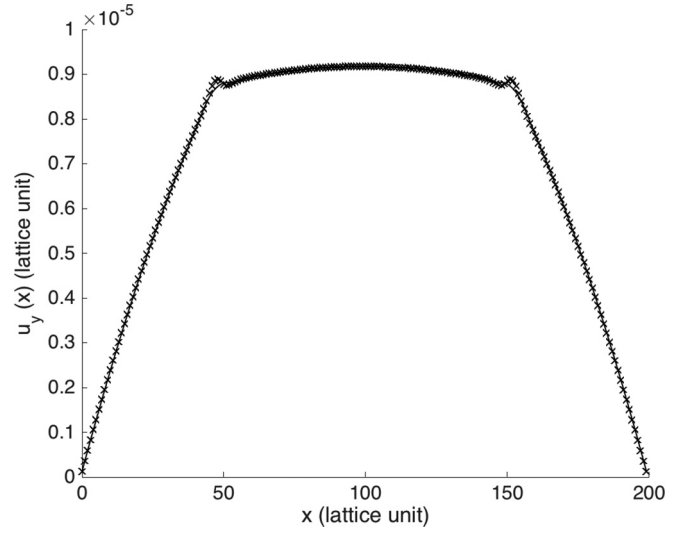

FIG. 2. Velocity variation for the test illustrated in Fig. 9. Simulation data are represented by crosses and semianalytic theory (which accounts for the transverse variation of the density) by the continuous line. For these data, $L_x = 200$, $\alpha_B = 0.2$, $\alpha_R = 0.9$, $\Lambda = 8$, $\nu_R = \nu_B = 0.333$, $\beta = 0.4$.

density difference effects [see Eqs. (5)], is identical to that for LBGK collision.

We consider here curved fluid-fluid interfaces, as well as plane interfaces. No assessment would be complete without some consideration of the interfacial microcurrent. For all the data presented below, we relax the ghost modes of our MRT scheme to equilibrium, i.e., $\lambda_7 = \lambda_8 = 1$.

A. Plane interfaces

The data in Fig. 2 compare simulation and theory. We test the steady-state of uni-directional, pressure-driven flow, with the transverse density stratification illustrated in Fig. 9. Note, we do not benchmark against the solution for discontinuous variation of density (see, e.g., Ba *et al.* [29]). Instead, we compare simulation data (crosses) with a semianalytical solution in Appendix D, which accounts for the effects of continuous variation of density at the interface (continuous line). For these data, the simulation width $L_x = 200$, $\alpha_B = 0.2$, $\alpha_R = 0.9$ (corresponding to a density contrast between separated components' bulk of $\Lambda = 8$) and $\nu_B = \nu_R = 0.333$. These data compare well with theory and data generated by identical tests applied to the MRT schemes of Ba *et al.* [29], which are based upon equivalent MCLBE interface schemes and traditional MRT collision operators. Note, however, that we find it necessary to use high order stencils of Appendix B to compute density gradients.

It is important to note that steady-state data in Fig. 2 do not verify instantaneous compliance with kinematic (impenetrability) and dynamic (continuous traction) conditions [14,39]. For that, one needs a transient flow. Semianalytical solutions for multicomponent flow with flat and curved interfaces, which reference the key boundary conditions at issue are derived in Appendix C.
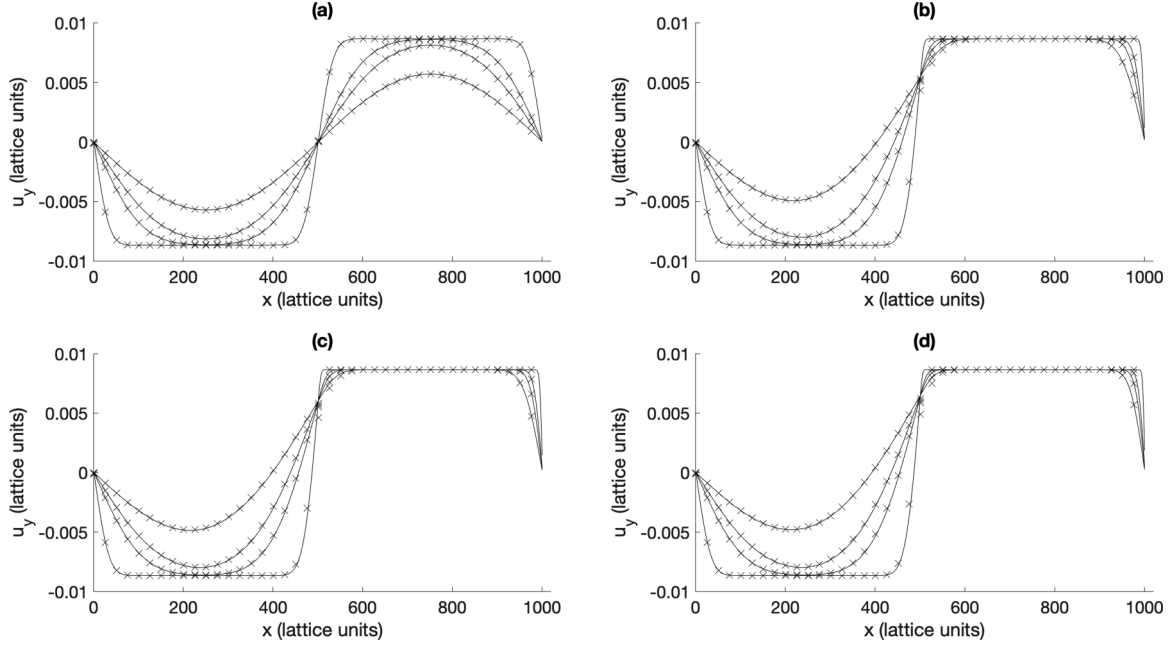
FIG. 3. Flow at a flat, sheared interface; comparison of simulation data (crosses) and a semianalytical solution (see Appendix C), for a large range of density contrasts, Λ. For these data, shear viscosity $\eta = 0.166$, while kinematic viscosity $\nu = \frac{\eta}{\rho}$ changes. The interface centers on $x = 500$ lattice units, with the fluid on the right the denser. The fluid on the left (right) is moving south (north) initially. For panels (a)–(d), $\Lambda = 1, 20, 31.25, 50$, respectively. These data confirm continuity of velocity and correct transmission of stress across a flat, sheared interface.

In Appendix C, we consider the temporal decay of unidirectional flows of two liquids of different density separated by a flat interface. The systems have defined initial velocity profile and the motion decays to rest. The geometry and flow initial conditions defining our tests are shown schematically in, e.g., Fig. 7. The density and, with it, the kinematic viscosity change at the interface, which is tangentially sheared. We have obtained analytical benchmarks for this problem, in the sharp interface limit, in Appendix C, using Sturm-Liouville theory [40] straightforwardly. Figure 3 compares simulation data (crosses) and the analytical solution, for a large range of density contrasts, Λ (see caption). For these data, shear viscosity $\eta = 0.166$ and segregation parameter $\beta = 0.5$ are constant whilst kinematic viscosity $\nu = \frac{\eta}{\rho}$ changes. This change is assumed discontinuous in Appendix C, whereas in simulation density varies across the interface. Even so, it is clear that these data confirm continuous operation of the continuous traction condition across the interface, not simply that the correct *steady-state* profile is obtained. This assertion is support by the data in Table II, which shows the domain-average, relative error between the semianalytic solution for

$u(x, t)$, and the simulated solution, $u^*(x, t)$,

$$\epsilon(t) = \frac{\sum_i |u(x_i, t) - u^*(x_i, t)|^2}{\max[u^*(x_i, t)]^2}, \qquad (18)$$

which never exceeds 1%. Above, x_i denotes the discrete, "on-lattice" value of the transverse coordinate. In Fig. 3 the denser fluid is on the right. Its greater density means that it is not accelerated by the traction of the fluid on the left, as strongly as the the fluid on the left is accelerated by the traction of the fluid on the right.

Note that data were matched between simulation and theory by equating the nondimensional groups which scale the MCLBE dynamics and the corresponding unidirectional Navier-Stokes equation [Eq. (C1)], as follows: $\frac{\nu(\lambda_3)^* T^*}{H^{*2}} = \frac{\nu T}{H^2}$, where the quantities with (without) asterisks are in lattice (physical) units. From this, we find the simulation time

TABLE II. Time variation of error $\epsilon(t)$ of Eq. (18).

	Lattice relative error (%)			
T(lu)	$\Lambda = 10$	$\Lambda = 20$	$\Lambda = 31.25$	$\Lambda = 50$
1000	0.299	0.560	0.754	0.979
10 000	0.114	0.199	0.252	0.300
20 000	0.080	0.135	0.167	0.196
50 000	0.047	0.075	0.092	0.115

TABLE III. Microcurrent activity for a range of separated components' density contrast. For these data, the interface curvature calculation [see Eq. (10)] has been replaced by assigning $K = \frac{1}{R}$. The full flow field for the case of $\Lambda = 10$ is shown in Fig. 4(a).

	MRT : Fixed K		
Λ	α_B	α_R	$|\mathbf{u}|_{\max} \times 10^5$
0.001	0.9995	0.5000	11.2
0.010	0.9950	0.5000	1.0
0.100	0.9500	0.5000	3.64×10^{-4}
10	0.5000	0.9500	1.32×10^{-4}
100	0.5000	0.9950	1.8
1000	0.5000	0.9995	7.8

TABLE IV. Microcurrent activity for a range of separated components' density contrast. The full flow field for the case of $\Lambda = 10$ is shown in Fig. 4(b). The curvature is calculated using stencils here.

MRT : Calculated K			
Λ	α_B	α_R	$|\mathbf{u}|_{\max} \times 10^5$
0.001	0.9995	0.5000	11.2
0.010	0.9950	0.5000	3.3
0.100	0.9500	0.5000	1.0×10^{-1}
10	0.5000	0.9500	1.8×10^{-2}
100	0.5000	0.9950	1.8
1000	0.5000	0.9995	7.8

corresponding to physical time T as

$$T^* = \frac{\nu}{\nu(\lambda_3)}\left(\frac{H^*}{H}\right)^2 T. \qquad (19)$$

B. Curved interfaces

Consider now curved interfaces in two dimensions.

The expected dependence of the interfacial pressure step on surface tension parameter, σ was, naturally, confirmed for the range of $\Lambda \in [10^{-3}, 10^3]$ (the range of data in Tables III and IV) and $\sigma \in [0, 0.2]$. We proceed to consider other tests.

1. Interfacial microcurrent

We study a red drop, initialized with radius $R = 60$, on a lattice of size 200×200, with periodic boundary conditions. An interfacial microcurrent is present in all MCLBE models—see Fig. 4. It has been argued [41] that microcurrent circulation is a "correct" hydrodynamic response to application of a force, or perturbation, which is not native to the continuum scale (where an interface is discontinuous). We return to this point shortly.

For the particular case of chromodynamic MCLBE, the spatial pattern of nonisotropic numerical errors not offset by pressure (density) changes drive a persistent circulation. The source of numerical error lies in derivatives, discretization error associated with the Chapman-Enskog and the recolor step. With an interface force, setting $K = \frac{1}{R}$ (i.e., circumventing a numerical calculation of K) after Eq. (10) significantly reduces microcurrent activity [41]. Figure 4 compares the microcurrent flow field, at $\Lambda = 10$, for calculated and fixed curvature drops. Flow field vectors are normalized in each plot. The flow in the case of fixed curvature is actually much weaker (refer to Tables III and IV) and more restricted to the interfacial region. We will return to this matter shortly.

With $\Lambda = 1$ (no density contrast), numerical error derives only from the interface force, with the dominant contribution arising from calculation of local interface curvature, K. In the presence of component density differences, we introduce a need to correct the dynamics, which, as we see in Sec. III, introduces strong interfacial density gradients. Evolution equation source terms which rely on numerical derivatives of density add error to that already present in the Lishchuk, or interface force. Here, we make a quantitative assessment of the impact of that additional error.
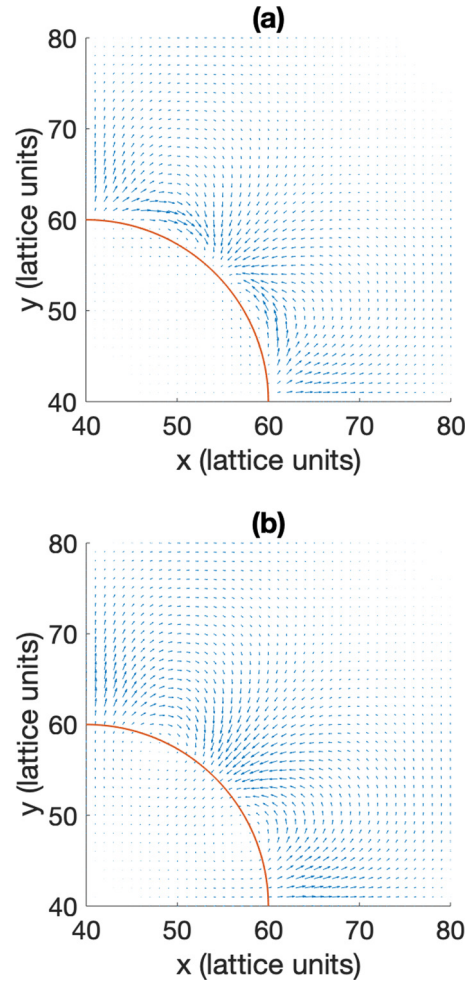

FIG. 4. Normalized microcurrent flow excerpt for $\Lambda = 10$ in the vicinity of a drop, radius $R = 20$ for (a) constant curvature $K = \frac{1}{R}$ and (b) numerically calculated curvature $K = \nabla_s \rho^N$. See Tables III and IV to scale these velocity fields. Note, the circulation in the case of fixed curvature [panel (a)] is more localized.

We present microcurrent data for a range of separated components' density contrast, Λ, in Tables III (fixed K) and IV. Based on the above discussion, the magnitude of the microcurrent depend on Λ (and, of course, $|\mathbf{G}|$), but is largely independent of collision scheme. This is confirmed in the data in Tables III and IV. (We note that changing the collision model to an LBGK scheme does not alter any of these data by more that a few percent.) For small Λ, when density contrast correction terms are small, the domain maximum microcurrent flow velocity magnitude, $|\mathbf{u}|_{\max} = \max(|\mathbf{u}|)$, is small. As the value of Λ increases (or decreases, in case of a rare drop) the microcurrent intensity increases.

For small Λ, the microcurrent regime is different, now being dominated by the interface force. First, we note a dramatic reduction in microcurrent recorded in both Tables III (fixed K) and IV, as interfacial density gradients reduce in size. Second, in comparing data for $\Lambda \in [10, 0.1]$ *between* Tables III (fixed K) and IV, we observe the signature reduction in microcurrent activity when we eliminate reliance on a K computed from second numerical gradients.
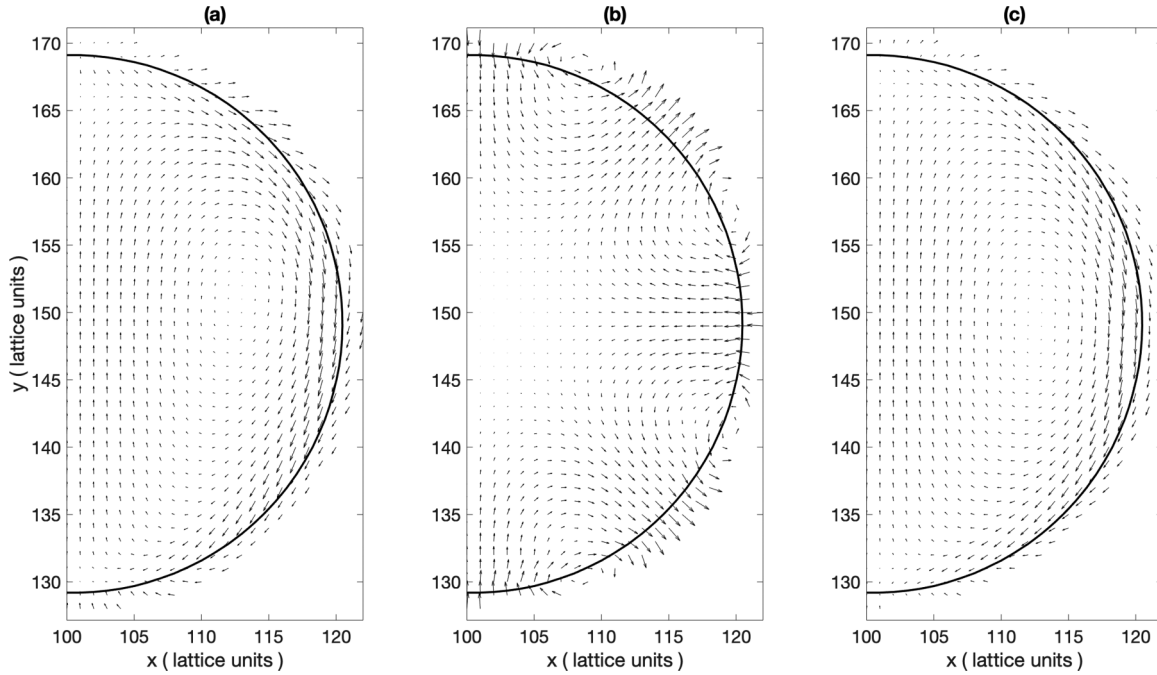
FIG. 5. Low Re internal flow past a tethered, cylindrical drop for $\Lambda = 5$. Flow outside the drop has been suppressed in these data. Panel (a) shows the total flow, in which the velocity field clearly has a nonphysical component perpendicular to the interface. Panel (b) shows the microcurrent error, measured from the frozen phase field from panel (a), without external flow, and panel (c) shows the physical flow exposed by subtracting the microcurrent in panel (b). The solid black line represents the center of the interface between the fluids ($\rho^N = 0$ contour). The internal flows are clearly parallel to the interface, as is the external flow (not shown).

For larger density contrasts, where the principal cause of the circulation is presumably density contrast, the data of Tables III and IV both comply with a scaling $|\mathbf{u_{max}}| \sim 7.4 \times 10^{-3} \Lambda$.

2. Kinematics of curved interfaces

Previous work [31] considered kinematics of a flat interface. Figure 5(c) shows the flow (once the microcurrent is subtracted), which is produced when blue fluid passes a tethered, cylindrical red drop, for density contrast $\Lambda = 5$. The Reynolds number must be kept very small here, to restrict deformation, and the drop is held spherical by large surface tension. Hence, these data correspond to the challenging regime of small Reynolds and capillary number. This accounts for the large microcurrent. The resulting Stokes' regime flow of internal and external fluid is apparently tangential to the curved interface at all points and continuous across it, i.e., we observe that, in the interfacial region, $v_n = 0$, $v_t =$ continuous. This accords with the kinematic condition of mutual impenetrability. Note that the flow in Fig. 5(c) is not the solved flow past a three-dimensional spherical drop.

3. Dynamics of curved interfaces

In Appendix C, we consider the temporal decay of a "unidirectional" flow of two liquids of different density separated by a curved interface. For this test, the system again has a defined initial velocity profile and the motion decays to rest. The geometry and flow initial conditions defining our test are shown schematically in Fig. 8. The assumed density and, with it, the kinematic viscosity change at the interface,

which is tangentially sheared. In all cases, the denser fluid is on the left, which accounts for its smaller acceleration. We have obtained an analytical solution for this problem, in the sharp interface limit in Appendix C, using adapted Sturm-Liouville theory. Figure 6 compares simulation data (crosses) and the analytical solution, for range of density contrasts, Λ (see caption) which is, note, smaller than that in Fig. 3. This reduction reflects the introduction of a curved interface. For these data, $R_0 = 120$, $R = 360$, shear viscosity $\eta = 0.333$ segregation parameter $\beta = 0.3$ are constant, while kinematic viscosity $\nu = \frac{\eta}{\rho}$ changes. This change is assumed discontinuous in the treatment of Appendix C, whereas in simulation density varies across the interface. Even so, these data confirm correct transient transmission of stress across the interface in our model, not simply that the correct *steady-state* profile is obtained.

Introduction of curvature undoubtedly reduces range of density contrast available to method whilst producing correct interfacial conditions but, in general, data presented in this section confirm that chromodynamic MRT schemes with density difference do recover correct boundary conditions at interface.

V. CONCLUSIONS

Using a single fluid formulation, we have developed a convenient, multiple-relaxation-time (MRT) collision scheme multicomponent lattice Boltzmann scheme (MCLBE) for simulating completely immiscible fluids with a density contrast, Λ, using the chromodynamic variant. Our technique is based upon the method of Dellar [35,36]. The model evolves a set of
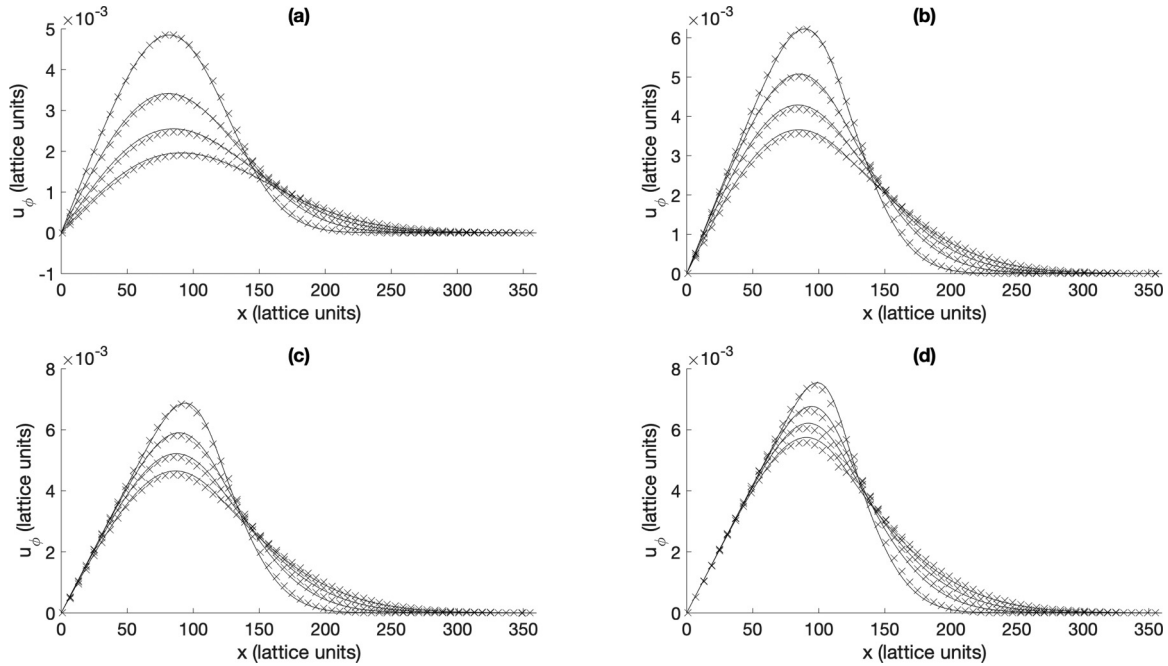
FIG. 6. Flow at a curved, sheared interface; comparison of simulation data (crosses) and semianalytical solution (see Appendix C) for a range of density contrasts, Λ. For these data, shear viscosity $\eta = $ constant, while kinematic viscosity $\nu = \frac{\eta}{\rho}$ changes. In all panels the interface centers on $r = 120$ lattice units, with fluid on the left the denser. The fluid on the left (right) is in uniform rotation (at rest), initially. For panels (a)–(d), $\Lambda = 1, 2, 3, 5$, respectively, which is smaller than the range of Λ shown in Fig. 3. These data confirm continuity of velocity and correct transmission of stress across a curved interface.

physical and nonphysical (ghost) modes of the system, equal in number to the cardinality of lattice basis set, then constructs an explicit distribution function *a posteriori*. We place all corrections to the target dynamics (the weakly compressible Navier-Stokes equations) in the kinetic-scale evolution equation. Significantly, the latter relies on density gradients, which can be large when Λ is large, which limits applications to moderate density contrast. We present in the appendices enhanced (but noncompact) stencils for gradient calculation which improve performance.

Equivalent MRT schemes, due to Ba *et al.* [29] and, earlier, Liu *et al.* [32] pioneered our essential approach. These authors showed the clear benefits of MRT collision models in benchmarking against complex flow simulations. To compliment this work, we focus, here, on fundamental, physical compliance in chromodynamic MCLBE MRT schemes. We produce data which compare well with the steady-state tests devised by Ba *et al.* [29], but also with new theory, as follows. We assess our model dynamics against semianalytical solutions to transient flow test cases which reference, explicitly, the kinematic condition of mutual impenetrability and dynamic interface boundary condition of continuous traction. Broadly, data compare well with these solutions, confirming satisfactory, instantaneous compliance with kinematic and dynamic conditions at the simulation interface.

While the Dellar-type MRT scheme we develop here is operationally equivalent to that of Ba *et al.*, it has an advantage. Practically, it has improved implementability—a post-collision distribution function is explicitly constructed from modes with simple, scalar relaxation. Theoretically, the connection between model kinematics and dynamics is

visible. This is a consequence of placing all density-difference dynamics corrections in the kinetic scale source term.

MCLBE MRT schemes are not without limitations: the well-known MCLBE interfacial microcurrent. Here our simulations of curved interfaces suggest that it may be removed completely from steady state simulations. Further, data presented for curved interfaces conform to our understanding of the interfacial microcurrent (see Ref. [41]), but the expected effect of dynamics corrective terms increases microcurrent activity associated with the method, roughly in proportion to Λ, with the contribution to the spurious signal greater than that arising from the surface tension perturbation for $\Lambda > 10$.

APPENDIX A: MULTIRELAXATION-TIME SCHEME FOR FORCED, DIPHASIC FLUIDS WITH LARGE DENSITY CONTRASTS

We derive the Navier-Stokes equations from the multiple-relaxation-time (MRT) lattice Boltzmann equation, adapted for multicomponent applications with a large density difference between completely immiscible components, where a body force is present. The latter is necessary to carry the interface force.

In the interest of a compact literature, we retain the overall structure of the analyses of Guo *et al.* [19], Dellar [35,36] and Hou *et al.* [42]. Our analysis, whilst based in $D2Q9$, generalizes straightforwardly. We choose to extend the scheme of Dellar because it is efficient (due to a careful choice of non-hydrodynamic modes N, J_x and J_y), robust, straightforward to implement and, not least, logical. In this section $\sum_i$ is used as an abbreviation for $\sum_i^{(Q-1)}$.

At the kinetic scale, the forced MRT LBE for a system subject to an "external" force term can be expressed as

$$
\begin{aligned}
f_i(\mathbf{x} + \mathbf{c}_i\delta_t, t + \delta_t) \\
= f_i(\mathbf{x}, t) + \sum_j A_{ij}\big[f_j^{(0)}(\mathbf{x}, t) - f_j(\mathbf{x}, t)\big] + \delta_t F_i, \quad \text{(A1)}
\end{aligned}
$$

where the density-difference supporting equilibrium which distributes mass away from the rest ($j = 0$) link via term ϕ_j, is in the form of

$$
f_j^{(0)} = \rho\phi_j + \rho w_j\left(3u_\alpha c_{j\alpha} + \frac{9}{2}u_\alpha u_\beta c_{j\alpha} c_{j\beta} - \frac{3}{2}u_\gamma u_\gamma\right), \quad \text{(A2)}
$$

and where the kinetic equation source term, F_i, is assumed to have the following properties,

$$
\sum_i (1, \mathbf{c}_i, \mathbf{c}_i\mathbf{c}_i)F_i = (0, n\mathbf{G}, \mathbf{C} + \mathbf{C}^T), \quad \text{(A3)}
$$

where scalar n and symmetric tensor, $(\mathbf{C} + \mathbf{C}^T)$, are to be determined.

We first set out the basics, then proceed to the Chapman-Enskog analysis to obtain the thermodynamic limit of the kinetic scheme defined in Eq. (A1) (i.e., find appropriate expressions for tensor $\mathbf{C}$, which represents the crux of the problem of recovering correct hydrodynamics with the MRT scheme), then we transform to a modal description, and finally, we invert that transformation to obtain an explicit expression for the post-collision distribution function.

To maintain parity with the analysis of Guo *et al.* [19] at the outset, we now relax the definition of lattice velocity in Eq. (7) as follows:

$$
\rho\mathbf{u} = \sum_i f_i(\mathbf{r}, t)\mathbf{c}_i + m\mathbf{G}, \quad \text{(A4)}
$$

with m a constant to be determined.

Dellar's [35,36] eigenvalues and corresponding left row eigenvectors for the collision matrix A_{ij} can be tabulated as in Table I, where we define

$$
\Pi_{\alpha\beta} \equiv \Pi_{\alpha\beta}^{(0)} + \Pi_{\alpha\beta}^{(1)}, \quad \text{(A5)}
$$

for $\alpha,\ \beta = x, y$, and the $\Pi_{\alpha\beta}^{(p)}$ have the usual meaning,

$$
\Pi_{\alpha\beta}^{(p)} = \sum_i f_i^{(p)} c_{i\alpha} c_{i\beta}, \quad p = 0, 1. \quad \text{(A6)}
$$

Mode $\Pi_{\alpha\beta}$ will be seen, shortly, to include the momentum flux and viscous stress tensors. As set-out in Table I, matrix A_{ij} has the following properties which, it will be seen, are necessary to recover correct hydrodynamics,

$$
\sum_i (1_i, c_{i\alpha}, c_{i\alpha}c_{i\beta})A_{ij} = (0, 0, \lambda_3 c_{j\alpha}c_{j\beta}). \quad \text{(A7)}
$$

Here α and β represent either x or y. We also assume that the lattice basis $\mathbf{c}_i$ and the corresponding weights w_i have

properties

$$
\sum_i w_i = 1, \quad \sum_i w_i(c_{i\alpha})^{2p+1} = 0, \quad p \geqslant 0,
$$

$$
\sum_i w_i c_{i\alpha}c_{i\beta} = \frac{1}{3}\delta_{\alpha\beta},
$$

$$
\sum_i w_i c_{i\alpha}c_{i\beta}c_{i\gamma}c_{i\theta} = \frac{1}{9}(\delta_{\alpha\beta}\delta_{\gamma\theta} + \delta_{\alpha\gamma}\delta_{\beta\theta} + \delta_{\alpha\theta}\delta_{\beta\gamma}), \quad \text{(A8)}
$$

where $\delta_{\alpha\beta}$ is the Kronecker δ. Weightings w_i are those of Qian *et al.* [43] and, later, Hou *et al.* [42]: $w_0 = \frac{4}{9}$, $w_{\text{odd}} = \frac{1}{36}$, $w_{\text{even}} = \frac{1}{9}$. Figure 1 shows our definition and indexing of links.

Note that the six left row eigenvectors $\mathbf{h}^{(0)}\cdots\mathbf{h}^{(5)}$, which appear in Eqs. (A7) and Table I, are linearly independent but not orthogonal. We will return to this matter. We follow Dellar [35,36] in selecting the other three "ghost" eigenvectors, or basis vectors (see Table I) as

$$
g_0 = 1, \quad g_{\text{odd}} = 4, \quad g_{\text{even}} = -2. \quad \text{(A9)}
$$

We note that Benzi *et al.* [44,45] used a qualitatively similar basis.

Our equilibrium distribution function $f_i^{(0)}$ may easily be shown to have the following necessary properties:

$$
\sum_i [1, c_{i\alpha}, c_{i\alpha}c_{i\beta}]f_i^{(0)}(\rho, \mathbf{u})
$$

$$
= [\rho, \rho u_\alpha, (2\phi_1 + 4\phi_2)\rho\delta_{\alpha\beta} + \rho u_\alpha u_\beta]. \quad \text{(A10)}
$$

Note, ϕ_1 and ϕ_2 depend upon the chromodynamic field [see Eq. (4)], so the spatial-temporal variation of the isotropic term of the second moment is modified: $\sum_i f_i^{(0)} c_{i\alpha}c_{i\beta} = \{\frac{3}{5}[(1 - \alpha_R)\rho_R + (1 - \alpha_B)\rho_B]\delta_{\alpha\beta} + \rho u_\alpha u_\beta\}$, with the variation of the speed of sound between blue components now apparent, since $c_{sR}^2 = \frac{3}{5}(1 - \alpha_R)$, $c_{sB}^2 = \frac{3}{5}(1 - \alpha_B)$.

We now proceed with a Chapman-Enskog expansion of the kinetic equation and distribution function. To reflect the changes occurring at different timescales, we write

$$
f_i = f_i^{(0)} + \epsilon f_i^{(1)} + \epsilon^2 f_i^{(2)} + \cdots, \quad \text{(A11)}
$$

$$
\frac{\partial}{\partial t} = \frac{\partial}{\partial t_0} + \epsilon\frac{\partial}{\partial t_1} + \epsilon^2\frac{\partial}{\partial t_2}\cdots \quad \text{(A12)}
$$

Parameter ϵ can be interpreted as the Knudsen number. Assuming that density and velocity are not to be expanded in ϵ, the assumptions in Eq. (A10) imply $\sum_i f_i^{(p)} = 0$ and $\sum_i f_i^{(p+1)}\mathbf{c}_i = 0$, ($p \geqslant 1$), but note Eq. (A4) implies $\sum_i f_i^{(1)}\mathbf{c}_i = -m\mathbf{G}\delta_t$.

Consider the most rapid behavior in the model. Applying the above expansions, we have

$$
O(\epsilon): \quad (c_{i\alpha}\partial_\alpha + \partial_{t_0})f_i^{(0)} = -\frac{1}{\delta_t}\sum_j A_{ij}f_j^{(1)} + F_i. \quad \text{(A13)}
$$

Summing (i.e., $\sum_i$) Eq. (A13) and using Eqs. (A3) and (A7),

$$
\frac{D}{Dt_0}\rho = 0. \quad \text{(A14)}
$$

For the counterpart result in the model kinematics, we use Eq. (15) as $\frac{D\rho_R}{Dt} = \frac{D\rho_B}{Dt} = 0$, from which [31],

$$\frac{D\rho^N}{Dt_0} = 0. \tag{A15}$$

Multiplying Eq. (A13) by c_{ix} (say), summing and using Eqs. (A3) and (A7) result in an Euler equation,

$$\partial_\alpha \Pi_{\alpha x}^{(0)} + \partial_{t_0} \rho u_x = nG_x. \tag{A16}$$

Equation (A16) differs from Eq. (10b) in Ref. [19], since the latter couples n, m, and τ (LBGK collision parameter). Here, we recover the appropriate Euler equation by setting $n = 1$ with, note, no constraint on m at $O(\epsilon)$.

At slower $O(\epsilon)^2$, the Chapman-Enskog expansion is

$$O(\epsilon^2): \partial_{t_1} f_i^{(0)} + (c_{i\alpha}\partial_\alpha + \partial_{t_0})f_i^{(1)}$$
$$- \frac{1}{2}(c_{i\alpha}\partial_\alpha + \partial_{t_0}) \sum_j A_{ij} f_j^{(1)}$$
$$= -\frac{1}{2}(c_{i\alpha}\partial_\alpha + \partial_{t_0})\delta_t F_i. \tag{A17}$$

Summing (i.e., $\sum_i$) Eq. (A17) and simplifying gives

$$\partial_{t_1} \rho = 0, \tag{A18}$$

having set $(m - \frac{n}{2}) = 0$. This is equivalent to Eq. (13a) of Ref. [19]. Constants m and n are now determined for our MRT scheme,

$$n = 1, \quad m = \tfrac{1}{2}. \tag{A19}$$

Multiply Eq. (A17) by c_{iy} (say), sum, identify the second-order moment using Eq. (A3), and use Eqs. (A7) and (A19),

$$\partial_{t_1}(\rho u_y) = \partial_\alpha \sigma_{\alpha y}', \tag{A20}$$

where the viscous stress tensor $\sigma_{\alpha y}'$ is

$$\sigma_{\alpha y}' = -\left(1 - \frac{\lambda_3}{2}\right)\Pi_{\alpha y}^{(1)} - \frac{\delta_t}{4}(C_{\alpha y} + C_{y\alpha}). \tag{A21}$$

Equation (A20) is the MRT equivalent of Eq. (13b) in Ref. [19]. (Our assignment $m = \frac{1}{2}$ accords with Guo *et al.* but their constraint $(n + \frac{m}{\tau}) = 1$ does not arise here.)

So far, our approach parallels that of Ref. [19] but our use of an MRT scheme means we must proceed to an expression for $\Pi_{\alpha\beta}^{(1)}$ via a second moment of Eq. (A13) (i.e., multiply by $c_{i\alpha}c_{i\beta}$ and sum). After algebra,

$$\lambda_3 \frac{\Pi_{\alpha\beta}^{(1)}}{\delta_t} = -\frac{2\rho}{3} S_{\alpha\beta} - u_\alpha(G_\beta - \partial_\beta\Phi') - u_\beta(G_\alpha - \partial_\alpha\Phi')$$
$$+ \left[u_\gamma \partial_\gamma \Phi' - \frac{1}{3}\rho \partial_\gamma u_\gamma\right]\delta_{\alpha\beta} + \frac{1}{2}(C_{\alpha\beta} + C_{\alpha\beta}), \tag{A22}$$

where $S_{\alpha\beta} = \frac{1}{2}(\partial_\alpha u_\beta + \partial_\beta u_\alpha)$, and we have defined

$$\Phi' = \tfrac{3}{5}(1 - \alpha_R)(\rho_R + \Lambda\rho_B) - \tfrac{1}{3}\rho. \tag{A23}$$

To obtain $\Pi_{\alpha\beta}^{(1)}$ in Eq. (A22), multiply Eq. (A13) by $c_{i\alpha}c_{i\beta}$, sum, substitute the definition of $f_i^{(0)}$ [Eq. (3)], use Eqs. (A7) to introduce eigenvalue λ_3, and, crucially, use Eq. (A15) (i.e.,

the model kinematics) to eliminate terms like $\frac{\partial}{\partial t_0}(2\phi_1 + 4\phi_2)$ [31]. That is, the form of $\Pi_{\alpha\beta}^{(1)}$ in Eq. (A22) relies on the fact that ρ^N is a material invariant, on the shortest timescales. Use the viscous stress definition, Eqs. (A21) and (A22), and simplify,

$$\frac{\sigma_{\alpha\beta}'}{\delta_t} = -\frac{1}{2\lambda_3}(C_{\alpha\beta} + C_{\beta\alpha}) + \frac{2}{3}\left(\frac{1}{\lambda_3} - \frac{1}{2}\right)\rho S_{\alpha\beta}$$
$$+ \left(\frac{1}{\lambda_3} - \frac{1}{2}\right)[u_\alpha(G_\beta - \partial_\beta\Phi') + u_\beta(G_\alpha - \partial_\alpha\Phi')]$$
$$- \left(\frac{1}{\lambda_3} - \frac{1}{2}\right)\left[u_\gamma \partial_\gamma \Phi' - \frac{1}{3}\rho\partial_\gamma u_\gamma\right]\delta_{\alpha\beta}. \tag{A24}$$

The discrepancy between the desired result (a term in $\rho S_{\alpha\beta}$) and Eq. (A24) defines an error,

$$E_{\alpha\beta} = -\frac{1}{2\lambda_3}(C_{\alpha\beta} + C_{\beta\alpha}) + \left(\frac{1}{\lambda_3} - \frac{1}{2}\right)[u_\alpha(G_\beta - \partial_\beta\Phi')$$
$$+ u_\beta(G_\alpha - \partial_\alpha\Phi')] - \left(\frac{1}{\lambda_3} - \frac{1}{2}\right)$$
$$\times \left[u_\gamma \partial_\gamma \Phi' - \frac{1}{3}\rho\partial_\gamma u_\gamma\right]\delta_{\alpha\beta}. \tag{A25}$$

Therefore, we make the following choice for $C_{\alpha\beta}$:

$$C_{\alpha\beta} = \left(1 - \frac{\lambda_3}{2}\right)[u_\alpha(G_\beta - \partial_\beta\Phi') + u_\beta(G_\alpha - \partial_\alpha\Phi')]$$
$$- \left(1 - \frac{\lambda_3}{2}\right)\left[u_\gamma \partial_\gamma \Phi' - \frac{1}{3}\rho\partial_\gamma u_\gamma\right]\delta_{\alpha\beta}, \tag{A26}$$

whence, from Eq. (A24), $\sigma_{\alpha\beta}' = \frac{2}{3}(\frac{1}{\lambda_3} - \frac{1}{2})\rho S_{\alpha\beta}\delta_t$, so our model's kinematic viscosity is $\nu = \frac{1}{6}(\frac{2}{\lambda_3} - 1)$. Further, we are also now able to write a local expression for the viscous stress in our large density difference model from Eqs. (A6) and (A21),

$$\sigma_{\alpha\beta}' = -\left(1 - \frac{\lambda_3}{2}\right)\sum_i f^{(1)}c_{i\alpha}c_{i\beta} + \frac{\delta_t}{4}(C_{\alpha\beta} + C_{\beta\alpha}), \tag{A27}$$

with $C_{\alpha\beta}$ defined in Eq. (A26). With this $C_{\alpha\beta}$, source F_i in Eq. (A1) is partitioned into a term responsible for correcting for density gradients associated with component changes, F_{1i}, and one for the interface force F_{2i},

$$F_i = F_{1i} + F_{2i}, \tag{A28}$$

where, conforming to Eq. (5),

$$T_{\alpha\beta} = \frac{1}{2c_s^4}\left(1 - \frac{\lambda_3}{2}\right)\left\{\frac{1}{3}\rho\partial_\gamma u_\gamma \delta_{\alpha\beta}\right.$$
$$\left. - (u_\alpha\partial_\beta\Phi' + u_\beta\partial_\alpha\Phi' + u_\gamma\partial_\gamma\Phi'\delta_{\alpha\beta})\right\}, \tag{A29}$$

and Eq. (6) gives F_{2i} (which differs significantly from that Guo *et al.* derive, for a uniform density LBGK).

We now turn to the modal projection. We encapsulate the collision source term within the evolution of the modes defined in Table I. In doing so, the advantages of Dellar's MRT scheme are preserved and we shall be able to produce

a collision step which is particularly implementable. Define matrix left row eigenvectors,

$$\mathbf{M} \equiv (\mathbf{h}^{(0)}, \mathbf{h}^{(1)}, \cdots, \mathbf{h}^{(8)})^T, \tag{A30}$$

such that

$$\mathbf{m} = \mathbf{M}\,\mathbf{f} = (\rho, \rho u_x, \rho u_y, \sigma_{xx}, \sigma_{yy}, \sigma_{xy}, N, J_x, J_y)^T. \tag{A31}$$

Equation (A1) is left multiplied by $\mathbf{M}$,

$$\mathbf{M}\,\mathbf{f}^+ = \mathbf{M}\,\mathbf{f} + \mathbf{M}\,\mathbf{A}\,\mathbf{M}^{-1}(\mathbf{M}\,\mathbf{f}^{(0)} - \mathbf{M}\,\mathbf{f}) + \mathbf{M}\,\mathbf{F}, \tag{A32}$$

where $\mathbf{F}$ denotes the column vector with elements F_i, and $\mathbf{f}$, $\mathbf{f}^+$, and $\mathbf{f}^{(0)}$ are column vectors. $\mathbf{h}^{(\mathbf{n})}$ are left (row) eigenvectors of $\mathbf{A}$, hence $\mathbf{M}\,\mathbf{A} = \mathbf{\Lambda}\,\mathbf{M}$, or

$$\mathbf{\Lambda} = \mathbf{M}\,\mathbf{A}\,\mathbf{M}^{-1}, \quad \mathbf{\Lambda} = diag(\lambda_0, \lambda_1, \cdots \lambda_8), \tag{A33}$$

where $\lambda_0 = \lambda_1 = \lambda_2 = 0$, $\lambda_3 = \lambda_4 = \lambda_5$, and $\lambda_7 = \lambda_8$. Therefore, Eq. (A32) may be written

$$m^{(p)+} = m^{(p)} + \lambda_p(m^{(0)(p)} - m^{(p)}) + S^{(p)},$$
$$p = 0, 1, .., (Q-1), \tag{A34}$$

the projection of F_i in Eq. (A1) giving modal source,

$$S^{(p)} = \sum_j M_{pj} F_j. \tag{A35}$$

We aim to determine the $S^{(p)}$, then to invert the transformation in Eq. (A32). Bearing in mind the structure of $\mathbf{M}$, it is straightforward to show

$$S^{(0)} = \mathbf{h}^{(0)} \cdot \mathbf{F} = \sum_i h_i^{(0)} F_i = A \equiv 0,$$

$$S^{(1)} = \mathbf{h}^{(1)} \cdot \mathbf{F} = \sum_i h_i^{(1)} F_i = \sum_i c_{ix} F_i = nF_x \delta_t,$$

$$S^{(2)} = \mathbf{h}^{(2)} \cdot \mathbf{F} = \sum_i h_i^{(2)} F_i = \sum_i c_{iy} F_i = nF_y \delta_t,$$

$$S^{(3)} = \mathbf{h}^{(3)} \cdot \mathbf{F} = \sum_i h_i^{(3)} F_i = \sum_i c_{ix}^2 F_i = C_{xx},$$

$$S^{(4)} = \mathbf{h}^{(4)} \cdot \mathbf{F} = \sum_i h_i^{(4)} F_i = \sum_i c_{iy}^2 F_i = C_{yy},$$

$$S^{(5)} = \mathbf{h}^{(5)} \cdot \mathbf{F} = \sum_i h_i^{(5)} F_i = \sum_i c_{ix} c_{iy} F_i$$
$$= \frac{1}{2}(C_{xy} + C_{yx}),$$

$$S^{(6)} = \mathbf{h}^{(6)} \cdot \mathbf{F} = \sum_i h_i^{(6)} F_i = \sum_i g_i F_i$$
$$= -\frac{1}{2}(C_{xx} + C_{yy}),$$

$$S^{(7)} = \mathbf{h}^{(7)} \cdot \mathbf{F} = \sum_i h_i^{(7)} F_i = \sum_i g_i c_{ix} F_i = 0,$$

$$S^{(8)} = \mathbf{h}^{(8)} \cdot \mathbf{F} = \sum_i h_i^{(8)} F_i = \sum_i g_i c_{iy} F_i = 0.$$

Note, source F_i has no projection onto the nonhydrodynamic modes N, J_x, J_y. Projections of $\mathbf{f}^{(0)}$ are also required:

$$\mathbf{h}^{(0)} \cdot \mathbf{f}^{(0)} = \sum_i h_i^{(0)} f_i^{(0)} = \sum_i 1_i f_i^{(0)} = \rho,$$

$$\mathbf{h}^{(1)} \cdot \mathbf{f}^{(0)} = \sum_i h_i^{(1)} f_i^{(0)} = \sum_i c_{ix} f_i^{(0)} = \rho u_x,$$

$$\mathbf{h}^{(2)} \cdot \mathbf{f}^{(0)} = \sum_i h_i^{(2)} f_i^{(0)} = \sum_i c_{iy} f_i^{(0)} = \rho u_y,$$

$$\mathbf{h}^{(3)} \cdot \mathbf{f}^{(0)} = \sum_i h_i^{(3)} f_i^{(0)} = \sum_i c_{ix}^2 f_i^{(0)} = \Pi_{xx}^{(0)}$$

$$\mathbf{h}^{(4)} \cdot \mathbf{f}^{(0)} = \sum_i h_i^{(4)} f_i^{(0)} = \sum_i c_{iy}^2 f_i^{(0)} = \Pi_{yy}^{(0)},$$

$$\mathbf{h}^{(5)} \cdot \mathbf{f}^{(0)} = \sum_i h_i^{(5)} f_i^{(0)} = \sum_i c_{ix} c_{iy} f_i^{(0)} = \Pi_{xy}^{(0)},$$

$$\mathbf{h}^{(6)} \cdot \mathbf{f}^{(0)} = \sum_i h_i^{(6)} f_i^{(0)} = \sum_i g_i f_i^{(0)}$$
$$= \frac{9}{5}\alpha_R \rho_R + \frac{9}{5}\alpha_B \rho_B - \frac{4}{5}\rho,$$

$$\mathbf{h}^{(7)} \cdot \mathbf{f}^{(0)} = \sum_i h_i^{(7)} f_i^{(0)} = \sum_i g_i c_{ix} f_i^{(0)} = 0,$$

$$\mathbf{h}^{(8)} \cdot \mathbf{f}^{(0)} = \sum_i h_i^{(8)} f_i^{(0)} = \sum_i g_i c_{iy} f_i^{(0)} = 0.$$

We now find from Eq. (A34) and Table I the following "forced" modal evolution equations:

$$i = 0: \quad \rho^+ = \rho, \tag{A36}$$

$$i = 1: \quad (\rho u_x)^+ = \rho u_x + nF_x \delta_t, \tag{A37}$$

$$i = 2: \quad (\rho u_y)^+ = \rho u_y + nF_y \delta_t, \tag{A38}$$

$$i = 3 \cdots 5: (\Pi_{\alpha\beta})^+ = \Pi_{\alpha\beta} - \lambda_3(\Pi_{\alpha\beta} - \Pi_{\alpha\beta}^{(0)})$$
$$+ \frac{\delta_t}{2}(C_{\alpha\beta} + C_{\beta\alpha}), \tag{A39}$$

$$i = 6: \quad N^+ = N - \lambda_6 N, \tag{A40}$$

$$i = 7, 8: \quad J_\alpha^+ = J_\alpha - \lambda_7 J_\alpha, \tag{A41}$$

where subscripts α, $\beta = x$, y. We note the simple form of the relaxation equations for $m^{(6)} \cdots m^{(8)}$, i.e., N, J_x, J_y, which for $\lambda_6 = \lambda_7 = 1$, reduce to $N^+ = J_x^+ = J_y^+ = 0$.

Having found the forced evolution equations for all the modes $m^{(p)}$, we turn at last to the inversion, from mode space, directly to obtain the distribution function. We define column vectors $\mathbf{k}^{(p)}$:

$$k_i^{(0)} = 2w_i - \frac{3}{2}w_i(c_{ix}^2 + c_{iy}^2), \tag{A42}$$

$$k_i^{(1)} = 3w_i c_{ix}, \tag{A43}$$

$$k_i^{(2)} = 3w_i c_{iy}, \tag{A44}$$

$$k_i^{(3)} = \frac{9}{2}w_i c_{ix}^2 - \frac{3}{2}w_i, \tag{A45}$$

$$k_i^{(4)} = \frac{9}{2}w_i c_{iy}^2 - \frac{3}{2}w_i, \tag{A46}$$

$$k_i^{(5)} = 9w_i c_{ix} c_{iy}, \tag{A47}$$

$$k_i^{(6)} = \frac{1}{4} g_i w_i, \tag{A48}$$

$$k_i^{(7)} = \frac{3}{8} g_i w_i c_{ix}, \tag{A49}$$

$$k_i^{(8)} = \frac{3}{8} g_i w_i c_{iy}. \tag{A50}$$

It is straightforward, using the isotropy lattice properties expressed in Eqs. (A7) to show the $\mathbf{k}^{(p)}$s have the property $\mathbf{h}^{(p)} \cdot \mathbf{k}^{(p')} = \delta_{pp'}$, and hence

$$\mathbf{M}^{-1} = (\mathbf{k}^{(0)}, \mathbf{k}^{(1)}, \cdots, \mathbf{k}^{(8)}). \tag{A51}$$

Having found $\mathbf{M}^{-1}$, it is now possible to reconstruct a post-collision distribution function vector $\mathbf{f}^+ = \mathbf{M}^{-1} \mathbf{m}^+$ which, on appeal to Eq. (A34), gives

$$
\begin{aligned}
f_i^+ &= (M)_{ij}^{-1} m_j^+ \\
&= w_i \Bigg\{ \left[2 - \frac{3}{2} (c_{ix}^2 + c_{iy}^2) \right] \rho + 3((\rho u_x)^+ c_{ix} + (\rho u_y)^+ c_{iy}) \\
&\quad + \frac{9}{2} (\Pi_{xx}^+ c_{ix}^2 + 2\Pi_{xy}^+ c_{ix} c_{iy} + \Pi_{yy}^+ c_{iy}^2) - \frac{3}{2} (\Pi_{xx}^+ + \Pi_{yy}^+) \\
&\quad + \frac{1}{4} g_i N^+ + \frac{3}{8} g_i (J_x^+ c_{ix} + J_y^+ c_{iy}) \Bigg\},
\end{aligned}
$$

with the $(\rho u_x)^+$, $(\rho u_y)^+$, ρ^+, Π_{xx}^+, Π_{xy}^+, Π_{yy}^+, N^+, J_x^+, and J_y^+ determined in Eqs. (A36)–(A41) above. Species or color is finally reallocated according to Eq. (12).

Sources $S^{(p)}$ which rely on kinetic equation source term F_i may require spatial numerical derivatives of, e.g., density. Computation of such derivatives is important for scheme stability and accuracy. The latter is enhanced by use of higher-order stencils, as discussed below.

APPENDIX B: HIGH-ORDER LATTICE STENCILS

It is possible to exploit lattice tensor isotropy, to develop noncompact stencils of any chosen order of accuracy for first gradient quantities. Thampi *et al.* have given a similar treatment of this essential approach [46] but based around the other gradient quantities (the Laplacian). Consider a scalar function denoted f. No confusion with the color-blind distribution function, f_i, should arise from use of this notation. A multivariate Taylor expansion, on the lattice, of function $f(\mathbf{r})$ may be written: $f(\mathbf{r} + N\mathbf{c}_i) = f(\mathbf{r}) + \sum_{n=1}^{\infty} \frac{N^n}{n!} (\mathbf{c} \cdot \nabla)^n f$. Taking moments of this expansion with $w_i c_{ix}$ and appealing to lattice properties Eq. (A8), we straightforwardly obtain

$$\sum_i w_i f(\mathbf{r} + N\mathbf{c}_i) c_{ix} = \frac{N}{3} \frac{\partial f}{\partial x} + \sum_{n=2}^{\infty} \frac{N^{(2n-1)}}{(2n+1)!} E_{(2n-1)}, \tag{B1}$$

where $N \in \mathbb{Z}^+$, and we define the *m*th error term

$$E_{(m)} = \left(\sum_{i=1}^{Q} w_i c_{ix} c_{i\alpha_1} c_{i\alpha_2} .. c_{i\alpha_m} \right) \left(\frac{\partial^m f}{\partial x_{\alpha_1} \partial x_{\alpha_2} ... \partial x_{\alpha_m}} \right). \tag{B2}$$

We do not need expressions for the $E_{(m)}$ to eliminate them.

Let us obtain a noncompact stencil for $\frac{\partial f}{\partial x}$, correct to (say) fifth order, using straightforward linear algebra methods. Take $N = 1, 2, 3$ in Eq. (B1) and truncate each equation at $n > 3$, to obtain three equations (one for each choice of N). These three equations may be written as follows:

$$
\begin{bmatrix}
\sum_i w_i f(\mathbf{r} + \mathbf{c}_i) c_{ix} \\
\sum_i w_i f(\mathbf{r} + 2\mathbf{c}_i) c_{ix} \\
\sum_i w_i f(\mathbf{r} + 3\mathbf{c}_i) c_{ix}
\end{bmatrix}
=
\begin{bmatrix}
\frac{1^1}{1!} & \frac{1^3}{3!} & \frac{1^5}{5!} \\
\frac{2^1}{1!} & \frac{2^3}{3!} & \frac{2^3}{5!} \\
\frac{3^1}{1!} & \frac{3^3}{3!} & \frac{3^5}{5!}
\end{bmatrix}
\begin{bmatrix}
\frac{1}{3} \frac{\partial f}{\partial x} \\
E_{(3)} \\
E_{(5)}
\end{bmatrix}.
\tag{B3}
$$

The inverse matrix of coefficients, $C_{ij} = \frac{i^{(2j-1)}}{(2j-1)!}$ exists and may be computed. Inverting the above, then, we find an expression for $\frac{\partial f}{\partial x}$ as

$$
\frac{\partial f}{\partial x} =
\begin{bmatrix}
\frac{9}{2} & -\frac{9}{10} & \frac{1}{10}
\end{bmatrix}
\begin{bmatrix}
\sum_i w_i f(\mathbf{r} + \mathbf{c}_i) c_{ix} \\
\sum_i w_i f(\mathbf{r} + 2\mathbf{c}_i) c_{ix} \\
\sum_i w_i f(\mathbf{r} + 3\mathbf{c}_i) c_{ix}
\end{bmatrix}.
\tag{B4}
$$

This approach may be adapted to yield expressions for gradients of chosen accuracy.

APPENDIX C: TRANSIENT MULTICOMPONENT FLOWS WITH TRANSVERSE DENSITY STRATIFICATION

We consider the semianalytic, transient flows used in Sec. IV. These are, essentially base states of perturbed flows such as those developed by Kao [47] and Yih [48], which we obtain, here, by straightforward application of Sturm-Liouville theory. We use similar methodology on two cases of unidirectional, density stratified flow tangent to, first, a flat interface, then, second, a curved interface. We assume the separated fluids have identical shear viscosity, $\eta_1 = \eta_2 = \eta$, so the only variation between their kinematic viscosities arises from density.

Consider flow $u(x, t)\hat{e}_y$, (see Fig. 7) with translational invariance in the y direction and no-slip boundaries at $x = 0, H$. The flow is modeled as being density stratified with interfacial boundary conditions introduced as matching conditions on the solution's two pieces. Using the Navier-Stokes equations, the problem is written

$$
\begin{aligned}
\rho(x) \frac{\partial}{\partial t} u(x, t) &= \frac{\partial}{\partial x} \left[\eta \frac{\partial}{\partial x} u(x, t) \right], \\
u(0) &= u(H) = 0,
\end{aligned}
\tag{C1}
$$

with matching conditions on $u(x, t)$ applied at $x = \frac{H}{2}$ (below). We seek $u(x, t)$, by modal projection on Sturm-Liouville eigenfunctions, ϕ_n, with eigenvalues, c_n [40],

$$u(x, t) = \sum_{n=1}^{\infty} \sigma_n e^{-c_n^2 t} \phi_n(x) \tag{C2}$$

(where σ_n is a constant to be determined), such that

$$
\begin{aligned}
\frac{d}{dx} \left(\eta \frac{d\phi_n(x)}{dx} \right) + c_n^2 \rho(x) \phi_n(x) &= 0, \\
\phi_n(0) = \phi_n(H) &= 0, \\
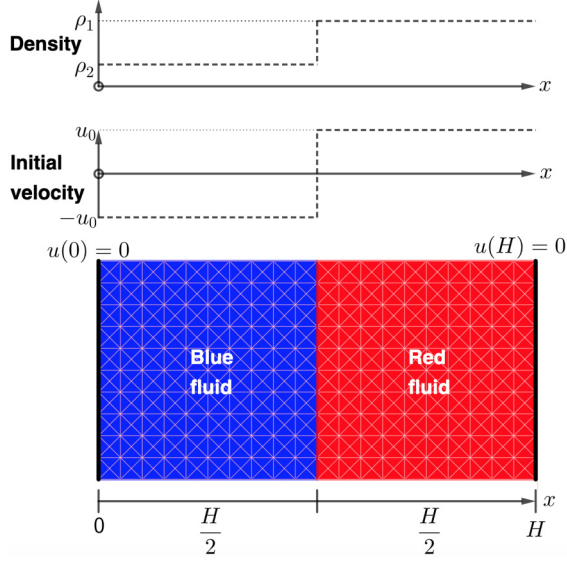\int_0^H \rho(x) \phi_n(x) \phi_m(x) dx &= \delta_{nm}.
\end{aligned}
\tag{C3}
$$

FIG. 7. Schematic. Geometry and initial conditions. Fluid is in unidirectional flow, $u(x)\hat{e}_y$. There is translational invariance in the y direction and density stratification, with the red (blue) fluid assumed to have density ρ_1 (ρ_2). Initially, the red (blue) fluid moves in the y ($-y$) direction.
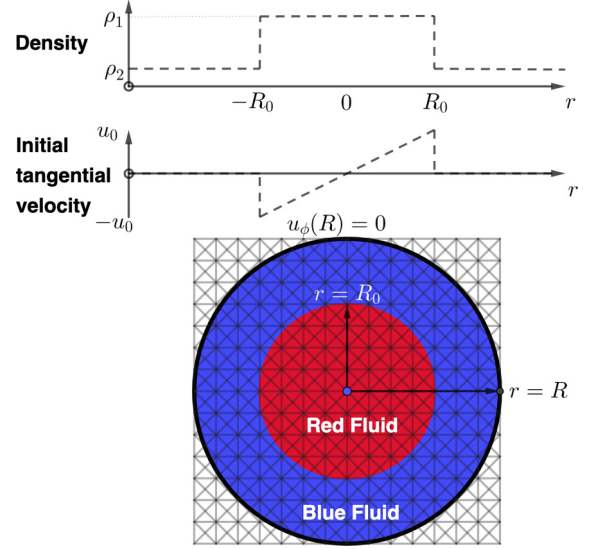

FIG. 8. Schematic. Geometry and initial conditions. A weakly compressible fluid is in rotational flow $u_\phi(r)\hat{e}_\phi$. r represents a "transverse" coordinate. A no-slip boundary is located at $r = [R]$. There is transverse density stratification with the red (blue) fluid having density ρ_1 (ρ_2). Initially, the red (blue) fluid moves in the $\hat{e}_\phi$ (is at rest).

ϕ_n is obtained piecewise, by solving Eq. (C3):

$$\phi_n^{(1)}(x) = A_n^{(1)} \sin\left(\frac{c_n}{\sqrt{\nu_1}}x\right), \quad x \in \left[0, \frac{H}{2}\right), \qquad \text{(C4)}$$

$$\phi_n^{(2)}(x) = A_n^{(2)} \sin\left(\frac{c_n}{\sqrt{\nu_2}}(x - H)\right), \quad x \in \left[\frac{H}{2}, H\right], \quad \text{(C5)}$$

where $A_n^{(1)}$ and $A_n^{(2)}$ are integration constants and $\nu_i = \frac{\eta}{\rho_i}$, $i = 1, 2$.

The kinematic condition $[\phi_n^{(1)}(H/2) = \phi_n^{(2)}(H/2)]$ and the continuous traction condition $([\phi_n^{(1)'}]_{H/2} = [\phi_n^{(2)'}]_{H/2})$ provide matching conditions via Eqs. (C4) and (C5)—for nontrivial $A_n^{(1)}$ and $A_n^{(2)}$,

$$\sqrt{\rho_2} \tan\left(\frac{c_n H}{2\sqrt{\nu_1}}\right) + \sqrt{\rho_1} \tan\left(\frac{c_n H}{2\sqrt{\nu_2}}\right) = 0. \qquad \text{(C6)}$$

By treating c_n as a continuous variable, this equation was solved using the Newton-Raphson method. Having thus determined the c_n, use the kinematic condition and the orthonormality property [Eq. (C3)], to show

$$A_n^{(1)} = 2\left\{\rho_1\left[H - \frac{\sqrt{\nu_1}}{c_n}\sin\left(\frac{c_n H}{\sqrt{\nu_1}}\right)\right]\right.$$
$$\left. + \frac{\sin^2\left(\frac{c_n H}{2\sqrt{\nu_1}}\right)}{\sin^2\left(\frac{c_n H}{2\sqrt{\nu_2}}\right)}\rho_2\left[H - \frac{\sqrt{\nu_2}}{c_n}\sin\left(\frac{c_n H}{\sqrt{\nu_2}}\right)\right]\right\}^{-1/2}, \quad \text{(C7)}$$

$$A_n^{(2)} = -A_n^{(1)}\frac{\sin\left(\frac{c_n H}{2\sqrt{\nu_1}}\right)}{\sin\left(\frac{c_n H}{2\sqrt{\nu_2}}\right)}. \qquad \text{(C8)}$$

Finally, we determine the σ_n, using the initial conditions

$$\sigma_n = A_n^{(1)}\frac{u_0}{c_n}\left\{\rho_1\sqrt{\nu_1}\left[1 - \cos\left(\frac{c_n H}{2\sqrt{\nu_1}}\right)\right]\right.$$
$$\left. - \rho_2\sqrt{\nu_2}\frac{\sin\left(\frac{c_n H}{2\sqrt{\nu_1}}\right)}{\sin\left(\frac{c_n H}{2\sqrt{\nu_2}}\right)}\left[1 - \cos\left(\frac{c_n H}{2\sqrt{\nu_2}}\right)\right]\right\}. \qquad \text{(C9)}$$

In summary, our transient flow's solution is defined by Eqs. (C2), (C7), and (C9).

We consider, now, flow in the axially symmetric geometry of Fig. 8. The initial condition is $u_\phi(r, 0) = r[\Theta(r) - \Theta(r - R_0)]$, the only nonzero strain rate is $\epsilon_{r\phi} = \frac{1}{2}\{r\frac{\partial}{\partial r}[\frac{1}{r}u_\phi(r, t)]\}$ and the fluid stress divergence is $\nabla \cdot \sigma = \frac{1}{r^2}\frac{\partial}{\partial r}(r^2\sigma_{r\phi})$. The fluids are Newtonian, with $\sigma_{r\phi} = 2\eta\epsilon_{r\phi}$. From the Navier-Stokes equations, therefore,

$$\rho(r)\frac{\partial}{\partial t}u_\phi(r, t) = \frac{1}{r^2}\frac{\partial}{\partial r}\left\{r^3\eta\frac{\partial}{\partial r}\left[\frac{1}{r}u_\phi(r, t)\right]\right\},$$
$$u_\phi(0, t) = u_\phi(R, t) = 0, \qquad \text{(C10)}$$
$$p_2 = p_1 + \frac{\sigma}{R_0},$$

with matching conditions applied at $r = R_0$.

Let $u_\phi(r, t) = \sum_{n=1}^{\infty}\sigma_n e^{-c_n^2 t}\phi_n(r)$, this time using a Sturm-Liouville eigenspectrum such that

$$\frac{d}{dr}\left[r\frac{d}{dr}\phi_n(r)\right] - \frac{1}{r}\phi_n(r) = -c_n^2\left(\frac{r}{\nu}\right)\phi_n(r),$$
$$\phi_n(0) = \phi_n(R) = 0, \qquad \text{(C11)}$$
$$\int_0^R r[\nu(r)]^{-1}\phi_n(r)\phi_m(r) = \delta_{nm}.$$

Above, we have used an integrating factor to reach Sturm-Liouville form and the weight function is $w(r) = \frac{r}{\nu} = \frac{r\rho(r)}{\eta} = r\nu(r)^{-1}$ [40]. $\phi_n(r)$ is obtained by solving Eq. (C11) (Bessel's equation with $n = 1$):

$$\phi_n^{(1)}(r) = A_n^{(1)} J_1\left(\frac{c_n r}{\sqrt{\nu_1}}\right), \quad r \in [0, R_0), \tag{C12}$$

$$\phi_n^{(2)}(r) = A_n^{(2)}\left[J_1\left(\frac{c_n r}{\sqrt{\nu_2}}\right) - B_n^{(2)} Y_1\left(\frac{c_n r}{\sqrt{\nu_2}}\right)\right], \quad r \in [R_0, R], \tag{C13}$$

with $B_n^{(2)} = \frac{J_1\left(\frac{c_n R}{\sqrt{\nu_2}}\right)}{Y_1\left(\frac{c_n R}{\sqrt{\nu_2}}\right)}$. We determine eigenvalues, c_n, using the kinematic and continuous traction conditions as $\phi_n^{(1)}(R_0) = \phi_n^{(2)}(R_0)$ and $\epsilon_{r\phi}^{(1)}|_{R_0} = \epsilon_{r\phi}^{(2)}|_{R_0}$, respectively. These provide matching conditions on $\phi_n(r)$ with a nontrivial solution provided $f\left(\frac{c_n R_0}{\sqrt{\nu_1}}\right) = 0$, where

$$
\begin{aligned}
f(X) = &-k_a J_1(X)\bigg[J_0(k_a X) - J_2(k_a X) \\
&- \frac{J_1(k_a k_b X)}{Y_1(k_a k_b X)} Y_0(k_a X) + \frac{J_1(k_a k_b X)}{Y_1(k_a k_b X)} Y_2(k_a X)\bigg] \\
&+ \left[J_1(k_a X) - \frac{J_1(k_a k_b X)}{Y_1(k_a k_b X)} Y_1(k_a X)\right][J_0(X) - J_2(X)].
\end{aligned}
\tag{C14}
$$

Above, $k_a = \sqrt{\frac{\nu_1}{\nu_2}}$, $k_b = \frac{R}{R_0}$.

Eigenvalues c_n were again obtained using Newton-Raphson iteration. Given a set of c_n, we can now write

$$
\begin{aligned}
A_n^{(1)} = \bigg[&\frac{1}{\nu_1^2} \int_0^{R_0} r\phi_n^{(1)}\phi_n^{(1)} dr \\
&+ \frac{1}{\nu_2^2} \frac{J_1\left(\frac{c_n R_0}{\sqrt{\nu_1}}\right)}{J_1\left(\frac{c_n R_0}{\sqrt{\nu_2}}\right) - B_n^{(2)}(R_0) J_1\left(\frac{c_n R_0}{\sqrt{\nu_2}}\right)} \int_{R_0}^{R} r\phi_n^{(2)}\phi_n^{(2)} dr \bigg]^{-\frac{1}{2}},
\end{aligned}
\tag{C15}
$$

which was obtained using Simpson's rule. Also,

$$A_n^{(2)} = A_n^{(1)} \frac{J_1\left(\frac{c_n R_0}{\sqrt{\nu_1}}\right)}{J_1\left(\frac{c_n R_0}{\sqrt{\nu_2}}\right) - B_n^{(2)}(R_0) J_1\left(\frac{c_n R_0}{\sqrt{\nu_2}}\right)}. \tag{C16}$$

Integration constants, σ_n, are determined using initial and orthonormality conditions on ϕ_n, as

$$\sigma_n = A_n^{(1)} \frac{\rho_1}{\eta} \int_0^{R_0} r^2 J_1\left(\frac{c_n r}{\sqrt{\nu_1}}\right) dr, \tag{C17}$$

which was again evaluated using Simpson's rule. The full transient flow was computed using Eqs. (D3), (D4), (D5), and (C17).

APPENDIX D: NUMERICAL SOLUTION OF STEADY, PRESSURE-DRIVEN FLOW WITH DENSITY STRATIFICATION

Consider the steady-state of the density stratified, unidirectional flow $u(x)\hat{e}_y$, shown in Fig. 9, now with a steady pressure
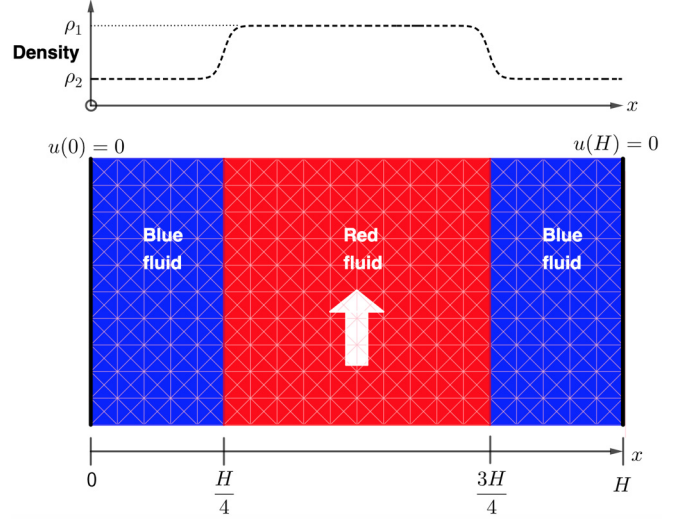

FIG. 9. Schematic representation of the geometry and transverse density stratification used in the pressure gradient (white arrow) driven flow tests.

gradient $(-G\hat{e}_y)$, a continuous transverse variation of density

$$
\begin{aligned}
\rho(x) = &\frac{1}{2}(\rho_{0R} + \rho_{0B}) \\
&+ \frac{1}{2}(\rho_{0R} - \rho_{0B}) \tanh\left[\beta\left(x - \frac{H}{4}\right)\right]\Theta\left(\frac{H}{2} - x\right) \\
&+ \frac{1}{2}(\rho_{0R} - \rho_{0B}) \tanh\left[\beta\left(\frac{3H}{4} - x\right)\right]\Theta\left(x - \frac{H}{2}\right),
\end{aligned}
\tag{D1}
$$

where $\Theta(x)$ is the Heaviside function. For this flow, the Navier-Stokes equation for a weakly compressible lattice fluid and the associated boundary and symmetry conditions are, respectively,

$$\frac{d}{dx}\left[\eta(x)\frac{d}{dx}u(x)\right] = G, \quad u(0) = u(H) = 0, \quad \left[\frac{du}{dx}\right]_{H/2} = 0, \tag{D2}$$

where ρ, u, and η again denote the density, velocity, and shear viscosity of the fluid, respectively. Note, shear viscosity, η, varies continuously with x when the kinematic viscosity, $\nu(\lambda_3) = $ constant, due to the variation in $\rho(x)$ identified in Eq. (D1). Let $x \leqslant \frac{H}{2}$. Integrating ordinary differential equation Eq. (D2) and eliminating the integration constant using the symmetry condition, we have

$$\frac{du}{dx} = \frac{G(2x - H)}{2\eta(x)}. \tag{D3}$$

Substituting $\eta(x) = \nu(\lambda_3)\rho(x)$, integrating over range $[0, x]$ with $x < \frac{H}{2}$, using the boundary condition $u(0) = 0$ and using a dummy variable, we

obtain

$$u(x) = \frac{G}{2\nu(\lambda_3)} \int_0^x \frac{(2\alpha - H)}{\rho(\alpha)} d\alpha. \qquad (D4)$$

The integral in Eq. (D4) was evaluated numerically, using Simpson's rule, using the expression for density given in Eq. (D1).

[1] A. K. Gunstensen, D. H. Rothman, S. Zaleski, and G. Zanetti, Phys. Rev. A **43**, 4320 (1991).

[2] S. Succi, *The Lattice Boltzmann Equation for Fluid Dynamics and Beyond* (Clarendon Press, Oxford, 2001).

[3] T. Kruger, H. Kusumaatmaja, A. Kuzmin, O. Shardt, G. Silva, and E. M. Viggen, *The Lattice Boltzmann Method, Principles and Practice* (Springer, Berlin, 2017).

[4] H. Huang, M. Sukop, and X. Lu, *Multiphase Lattice Boltzmann Methods: Theory and Application* (John Wiley & Sons, New York, 2015).

[5] D. H. Rothman and J. M. Keller, J. Stat. Phys. **52**, 1119 (1988).

[6] D. H. Rothman and S. Zaleski, *Lattice Gas Cellular Automata, Collection Aléa-Saclay* (Cambridge University Press, Cambridge, UK, 1994).

[7] D. Raabe, Model. Simul. Mater. Sci. Eng. **12**, 13 (2004).

[8] M. R. Swift, W. R. Osborn, and J. M. Yeomans, Phys. Rev. Lett. **75**, 830 (1995).

[9] M. R. Swift, E. Orlandini, W. R. Osborn, and J. M. Yeomans, Phys. Rev. E **54**, 5041 (1996).

[10] A. J. Wagner, Phys. Rev. E **74**, 056703 (2006).

[11] Q. Li and A. J. Wagner, Phys. Rev. E **76**, 036701 (2007), and references therein.

[12] A. J. Wagner and C. M. Pooley, Phys. Rev. E **76**, 045702(R) (2007), and references therein.

[13] X. Shan and H. Chen, Phys. Rev. E **49**, 2941 (1994).

[14] L. Landau and E. M. Lifshitz, *Fluid Mechanics*, 6th ed. (Pergamon Press, Oxford, UK, 1966).

[15] S. V. Lishchuk, C. M. Care, and I. Halliday, Phys. Rev. E **67**, 036701 (2003).

[16] J. U. Brackbill, D. B. Kothe, and C. Zemach, J. Comput. Phys. **100**, 335 (1992).

[17] U. D'Ortona, D. Salin, M. Cieplak, R. B. Rybka, and J. R. Banavar, Phys. Rev. E **51**, 3718 (1995).

[18] C. S. Peskin, Acta Numerica **11**, 479 (2002).

[19] Z. Guo, C. Zheng, and B. Shi, Phys. Rev. E **65**, 046308 (2002).

[20] T. Reiss and T. N. Phillips, J. Phys. A **40**, 4033 (2007).

[21] T. Reiss and P. J. Dellar, Comput. Fluids **46**, 417 (2011).

[22] T. Reiss, SIAM J. Sci. Comput. **40**, B1495 (2019).

[23] I. Halliday, A. P. Hollis, and C. M. Care, Phys. Rev. E **76**, 026708 (2007).

[24] X. Xu, K. Burgin, M. A. Ellis, and I. Halliday, Phys. Rev. E **96**, 053308 (2017).

[25] D. Kehrwald, Ph.D. thesis, Fraunhofer-Institut fur Techno- und Wirtschaftsmathematik, 2002.

[26] A. Subhedar, A. Reiter, M. Selzer, F. Varnik, and B. Nestler, Phys. Rev. E **101**, 013313 (2020).

[27] H. Liu, Y. Ju, N. Wang, G. Xi, and Y. Zhang, Phys. Rev. E **92**, 033306 (2015).

[28] S. Leclaire, N. Pellerin, M. Reggio, and J.-Y. Trépanier, J. Phys. A **47**, 105501 (2014).

[29] Y. Ba, H. Liu, Q. Li, Q. Kang, and J. Sun, Phys. Rev. E **94**, 023310 (2016).

[30] Z. X. Wen, Q. Li, Y. Yu, and Kai H. Luo, Phys. Rev. E **100**, 023301 (2019).

[31] K. Burgin, J. Spendlove, X. Xu, and I. Halliday, Phys. Rev. E **100**, 043310 (2019).

[32] H. Liu, A. J. Valocchi, and Q. Kang, Phys. Rev. E **85**, 046309 (2012).

[33] L.-S. Luo, Phys. Rev. Lett. **81**, 1618 (1998).

[34] I. Halliday, X. Xu, and K. Burgin, Phys. Rev. E **95**, 023301 (2017).

[35] P. J. Dellar, Phys. Rev. E **65**, 036309 (2002).

[36] P. J. Dellar, J. Comput. Phys. **190**, 351 (2002).

[37] M. Junk, Numer. Methods Differ. Equ. **17**, 383 (2001).

[38] P. Lallemand and L.-S. Luo, Phys. Rev. E **61**, 6546 (2000).

[39] J. Happel and H. Brenner, *Low Reynolds number hydrodynamics with special applications to particulate media*, 2nd ed. (Noordhoff, Leyden, 1973).

[40] G. Arfken, *Mathematical Methods for Physicists*, 2nd ed. (Academic Press, New York, 1970).

[41] I. Halliday, S. V. Lishchuk, T. J. Spencer, K. Burgin, and T. Schenkel, Comput. Phys. Commun. **219**, 286 (2016).

[42] S. Hou, Q. Zou, S. Chen, G. Doolen, and A. C. Cogley, J. Comput. Phys. **118**, 329 (1995).

[43] Y. H. Qian, D. d'Humières and P. Lallemand, Europhys. Lett. **17**, 479 (1992).

[44] R. Benzi, S. Succi, and M. Vergassola, Phys. Rep. **222**, 145 (1992).

[45] R. Benzi, S. Succi, and M. Vergassola, Europhys. Lett. **13**, 727 (1990).

[46] S. P. Thampi, S. Ansumali, R. Adhikari, and S. Succi, J. Comput. Phys. **234**, 1 (2013).

[47] T. W. Kao, Phys. Fluids **8**, 812 (1965).

[48] C.-S. Yih, J. FLuid. Mech. **27**, 337 (1967).